

Fast Physical Optics Calculation for SAR Imaging of Complex Scatterers

A Thesis

Presented in Partial Fulfillment of the Requirements for the Degree
Master of Science in the Graduate School of The Ohio State
University

By

Yuanhong Zhao, B.S.

Graduate Program in Electrical and Computer Engineering Department

The Ohio State University

2012

Master's Examination Committee:

Prof. Jin-Fa Lee, Advisor

Prof. Fernando Teixeira

© Copyright by

Yuanhong Zhao

2012

Abstract

The physical optics (PO) approximation is often used to compute the scattering from electrically large, perfectly conducting (PEC) objects. In order to generate the SAR image, the scattered field data from a large range of aspect angles and frequencies are needed. To quickly generate those data for SAR imaging system, several methods are used to accelerate the PO calculation. There are: (1) multi-level Z-buffering for self-shadowing calculation provides a low computation and accurate solution for complex scatterers, (2) Gordon's method converts the PO far field integral into simpler line integral on the flat surfaces, (3) accelerated frequency and angular sampling technique by partitioning the whole object into smaller domains is used to reduce the number of sampling points from direction computations. Theoretically, the complexity of computing all the spectrum for imaging system has been reduced from $O((k_{max}R)^4)$ to $O((k_{max}R)^3)$ if the mesh size is proportional to wavelength and (4) Fourier interpolation of the spectrum from polar grid to Cartesian grid. And a periodic extension for Fourier interpolation is employed to remedy the Gibb's phenomenon. Finally, the results of the complex object: ZSU-23-4 tank and F-16 fight jet with different frequency bands and elevation angles show the utility of combining these methods, which typically have been applied individually.

Dedicated to my family and my husband . . .

Acknowledgments

Foremost, I must thank my advisor Professor Jin-Fa Lee for providing me a great opportunity to join his group at the ElectroScience Lab, who showed me the most wonderful top class research on Computational Electromagnetics. He taught me not only how to be a true scholar but also a rigorous attitude for all the work not limited to the research area. This thesis cannot be done without his numerous guidance and patience in the past three years. Also I am sincerely grateful for the help from Dr. Peng Zhen, with whom I had lots of inspiring discussions and support.

Throughout the last three years my stay at the ElectroScience Lab, I learned a lot from several professors: Prof. Prabhakar Pathak, Prof. Fernando Teixeira, Prof. Robert Burkholder both from their EM classes and attitudes toward research. Besides, I thank all the fellows at the lab: Dr. Shao Yang, Xiaochuan Wang, Stylianos Dosopoulos, Jorsh Mahaffy, Caleb Waltz, Jue Wang, Jiangong Wei and Feng Wang for their friendship and the interesting discussions. Furthermore, I need to thank Kheng Hwee Lim to teach me how to use Solidworks and help me create the tank model. And many thanks to the sponsors from Singapore DSO lab especially Dr. Chia Tse Tong for his inspiring comments on my work.

At last, I thank my parents and sister for their endless support and love through my life. And for my husband Matt Stephanson, he has set a higher standard as an excellent graduate student and a qualified partner for me. I want to express my

deepest thanks for his unconditional emotional support and patience for my study
and my life.

Vita

July 01, 1987 Born - Shenyang, China

July, 2009 B.S. Electrical Engineering

September, 2009-present Graduate Research Associate,
ElectroScience Lab

Publications

Instructional Publications

Y.H. Zhao, M.B. Stephanson, Z. Peng and J.-F. Lee, “Helicopter Rotor Modulation Effects on Antenna Radiation and Scattering Problem,” 2011 IEEE AP-S/URSI International Symposium, Spokane, US.

Fields of Study

Major Field: Computational Electromagnetics

Table of Contents

	Page
Abstract	ii
Dedication	iii
Acknowledgments	iv
Vita	vi
List of Tables	ix
List of Figures	x
1. Introduction	1
1.1 Introduction	1
1.2 Review of high frequency asymptotic methods for SAR imaging . .	5
1.3 Reviews of imaging models	7
1.3.1 Prony's method	8
1.3.2 Auto-Regressive Moving Average (ARMA) model	11
1.3.3 Pencil of functions and Matrix Pencil (MP) Method	12
1.3.4 MUtiple SIgnal Classification (MUSIC) algorithm and Estimation of Signal Parameters via Rotational Invariance Technique (ESPRIT)	14
1.3.5 Other imaging methods	16
2. Physical Optics with Self-shadowing Technique	18
2.1 Physical Optics	18
2.2 Self-shadowing Technique	19

3.	Farfield Integration for Physical Optics	27
3.1	Far-field integral with PO approximation	27
3.2	Gordon's method	28
3.3	Accelerated Frequency Sampling	31
3.4	Multi-Frequency Multi-Angle Acceleration	36
4.	Synthetic Aperture Radar Imaging	42
4.1	Introduction to SAR Imaging	42
4.2	Polar to Cartesian Grid Interpolation	47
5.	Numerical Results	53
5.1	Image for simple object	53
5.2	SAR image for ZSU-23-4	55
5.3	SAR image of f-16	58
6.	Conclusions	61
	Appendices	62
A.	Proof for Gordon's method	62
	Bibliography	63

List of Tables

Table	Page
2.1 Computation time on lit region identification with Z-buffer algorithm.	24
3.1 Far-field evaluation time for ZSU-23-4	31
5.1 Computation time on lit region identification with Z-buffer algorithm.	58
5.2 Computation time on SAR imaging for f-16.	60

List of Figures

Figure	Page
2.1 (a) Physical equivalent for scattering by a PEC. (b) Approximate physical equivalent for scattering from a PEC.	19
2.2 Surface currents computed by conventional PO method of ZSU at 2 GHz	20
2.3 Z-buffering projection	21
2.4 Multi-level quad tree partitioning on the projection plane.	22
2.5 Identification of hidden surfaces for one triangle	23
2.6 Surface currents computed by the improved PO method of ZSU at 2 GHz	24
2.7 Computation time of self-shadowing algorithm for ZSU-23-4 at different frequencies.	25
2.8 (a)Comparison of VV scattered fields of the ZSU at 2 GHz with 30° elevation angle. (b)Comparison of HH scattered fields of the ZSU at 2 GHz with 30° elevation angle.	26
3.1 Surface currents computed by the improved PO method of ZSU at 2 GHz	29
3.2 Scattering pattern from smaller domains	32
3.3 Comparison between the interpolated and direct computed scattered field for ZSU-23-4 at 2 GHz.	34
3.4 Fast frequency acceleration for 1 meter sphere from 12 MHz to 3 GHz with top incident plane wave.	35

3.5	Fast frequency acceleration for 1m*1m*1m cube from 12 MHz to 3 GHz with $\theta = 45^\circ$, $\phi = 45^\circ$ incident plane wave.	35
3.6	Comparison between the interpolated and direct computed scattered field for ZSU-23-4 at 2 GHz.	36
3.7	Multi-frequency multi-angle acceleration for sphere from 12 MHz to 2 GHz. (a) Absolute error with $C_f = 2.0$, $C_a = 2.0$. (b) Absolute error with $C_f = 3.0$, $C_a = 3.0$	38
3.8	Multi-frequency multi-angle acceleration for cube from 12 MHz to 2 GHz (a) Absolute error with $C_f = 2.0$, $C_a = 2.0$. (b) Absolute error with $C_f = 3.0$, $C_a = 3.0$	38
3.9	Computation time for a sphere with different maximum frequencies. .	39
4.1	Illustration of down range imaging.	42
4.2	Illustration of cross range imaging.	43
4.3	Illustration of 2D SAR imaging system.	45
4.4	2D spectrum for SAR imaging in $k_x - k_y$ domain.	46
4.5	Illustration of interpolation from Polar to Cartesian grid data. . . .	47
4.6	Interpolation with Fourier harmonics for sphere from 10 MHz to 1 GHz. .	49
4.7	Even half-range periodic extension.	50
4.8	Interpolation with periodic extension for a sphere from 10 MHz to 1 GHz.	51
4.9	(a) Image generated without periodic extension for ZSU-23-4 with $f_{max} = 1 \text{ GHz}$. (b) Image generated with periodic extension for ZSU-23-4 with $f_{max} = 1 \text{ GHz}$	52
5.1	Image for a sphere with 1 meter radius.	54
5.2	Image for a 1m*1m*1m cube.	54

5.3	(a) Image generated from direct computation for ZSU-23-4 with $f_{max} = 1 \text{ GHz}$. (b)Image generated from 2D acceleration algorithm for ZSU-23-4 with $f_{max} = 1 \text{ GHz}$.	56
5.4	(a)Image for ZSU-23-4 with 0° elevation angle from 12 MHz to 1 GHz (b)Image for ZSU-23-4 with 0° elevation angle from 12 MHz to 4 GHz (c)Image for ZSU-23-4 with 0° elevation angle from 12 MHz to 8 GHz (d)Image for ZSU-23-4 with 20° elevation angle from 12 MHz to 8 GHz	57
5.5	(a)f-16 geometry for SAR imaging. (b)Image for f-16 with 0° elevation angle from 12 MHz to 1 GHz.	59
5.6	(a)Image for f-16 with 0° elevation angle from 12 MHz to 4 GHz. (b)Image for f-16 with 20° elevation angle from 12 MHz to 4 GHz.	60

Chapter 1: Introduction

1.1 Introduction

The application of synthetic aperture radar (SAR) imaging techniques for complex scatterers has attracted attention for several decades. These techniques are of great importance for remote sensing and target recognition. There are two well-known methods to verify the SAR imaging algorithm or to train an automatic target recognition system: perform measurements of the real target or simulating the scattered field of the target in a 2D parameter space using numerical methods. The real measurements are directly received by the antennas mounted on a moving platform to repetitively collect echo waveforms from the target. This whole process can provide good results, but it is tremendously expensive to take all of the measurements. As an alternative, numerical methods show advantages in terms of time and actual cost. Among all of these methods, rigorous ones such as method of moments (MoM), finite difference time domain (FDTD) method or finite element method (FEM) can produce exact solutions for scattered field. However, when dealing with electrically large structures, and particularly in this application for the SAR imaging, they are barely able to generate all the needed data over a certain range of aspects and frequency because of the computational costs in high frequency range. On the other hand,

asymptotic methods can maintain accuracy in high frequency range without increasing the computational costs. Physical Optics (PO) is widely used to approximate the high-frequency scattering from electrically large, perfectly electrically conducting (PEC) objects illuminated by an incident electromagnetic wave. So in this paper, we will focus on generating SAR image based on a fast and more efficient PO forward solver.

The PO approximation takes the contribution of the reflections from flat plates without considering diffractions, multiple bounces, or creeping waves. The equivalent currents on the surface are represented as $2\hat{n} \times \vec{H}_{inc}$ in the lit region and the equivalent current is 0 in the shadow region. Noted that incident magnetic field is \vec{H}_{inc} and \hat{n} is the unit surface normal pointing outwards. The entire object is divided into lit regions and shadow regions depending on the visibility from the incident wave direction. In the conventional PO method, the way to judge whether a particular part of the surface is lit or shadowed is just based upon a simple dot product of the incident wave vector k with the normal direction of each facet,

$$\begin{cases} \hat{k} \cdot \hat{n} < 0, & \text{lit region} \\ \text{otherwise}, & \text{shadow region} \end{cases} \quad (1.1)$$

However, this only applies to simple convex scatterers and does not take into account the object casting a shadow on itself. The effect of self-shadowing can be addressed by a few methods, for instance, analyzing all the surfaces through ray-tracing technique: angular Z-buffer algorithm [1, 2] or processing all the surfaces with Graphic Processing Unit (GPU) [3, 4]. In this paper, a multi-level Z-buffer algorithm, which can achieve a complexity close to $O(N)$, where N is the total number of triangles in the geometrical discretization, will be introduced in Chapter 2.

Once the PO current is determined, the mono-static scattered field in the far-field zone is calculated as

$$\vec{E}_{far}(\vec{r}) = \frac{j\omega\mu}{4\pi} \frac{e^{-jkr}}{r} \int_{\Gamma_{lit}} (\hat{k}^i \times \vec{J} \times \hat{k}^i) \cdot e^{-jk\hat{r}\cdot\vec{r}'} d\vec{r}'. \quad (1.2)$$

The oscillatory kernel $e^{-jk\hat{r}\cdot\vec{r}'}$ can be evaluated in the following few ways: the most traditional way to evaluate the PO integral is using Gaussian quadrature, but the distribution of quadrature points needs to obey the Nyquist sampling rate, so the cost of evaluating the integral in (1.2) is proportional to the wavenumber squared. The alternative to evaluate the integral is to use Gordon method [5] to convert the integral on the flat surface into analytical line integrals. With this method, if the current discretization can accurately represents the geometry then the flat surfaces don't have to be refined in terms of wave number, so the integration complexity becomes independent of the frequency.

With self-shadowing technique and Gordon's method, the scattered field can be calculated for a single incident angle and frequency. In order to get the image for a 2D object, the scattered field needs to be sampled according to Nyquist rate over a certain frequency and angular bandwidth that depends on the size of the object and the desired resolution. The Nyquist rate for the frequency sampling is $4f_{max}R/c$, where R is the radius of whole object's bounding sphere. Similarly, as the aspect angle sweeps from 0 to 2π , the angular Nyquist rate is $4f_{max} \cdot (2\pi)R/c$. Thus, the number of frequency and angular samples is $O(f_{max}^2 R^2)$. Conventionally, if a quadrature rule is used to evaluate the far-field integral, then the size of each triangle in the mesh should be proportional to λ^2 . So, the number of triangles, and therefore the cost to evaluate the integral once, is also $O((f_{max}R)^2)$. Putting all these estimates together,

the complexity of calculating all the necessary far field samples is $O[(f_{max}R)^4]$. This high complexity makes it a heavy burden to collect all the data for imaging system.

In this paper, we will reduce the sampling number from direct computation by partitioning the whole object into smaller domains and then interpolating each local scattering pattern to the entire scattering pattern. The far field integral is evaluated over each sub-domain individually, for a cost of $O[(f_{max}r)^2]$, where r is the radius of sub-domain's bounding sphere. Then the scattering pattern from the small domains are efficiently aggregated together to obtain the scattered field for the entire object. With this fast PO sampling strategy, the whole complexity of collecting radar data can be reduced from $O[(f_{max}R)^4]$ to $O[(f_{max}R)^3]$ when the mesh size is proportional to λ .

The whole thesis is organized as follows: first in Chapter 1, there is a brief review on the SAR imaging methods both on the high frequency solver side and the signal processing side; In Chapter 2, the Z-buffering technique is introduced to accurately identify the shadow region, and a multi-level quad tree partitioning strategy is used to enhance the efficiency of computing; In Chapter 3, the PO far-field integral is evaluated to get the scattering pattern. A multi-frequency multi-angle acceleration algorithm will be introduced to quickly achieve 2D scattering pattern for imaging system. Chapter 4 will present the imaging algorithm and the implementation on the Polar to Cartesian grid interpolation. All the numerical results will be given in Chapter 5 for a ZSU-23-4 model and F-16 fight jet, based on the 2-D IFFT algorithm.

1.2 Review of high frequency asymptotic methods for SAR imaging

The application of high frequency asymptotic methods in SAR imaging system is the key to provide spectrum in the frequency domain so as to verify the imaging algorithm. Several high frequency methods addressing different EM wave species have been successfully employed for SAR imaging.

At the very beginning, first order reflection is predicted by Physical Optics (PO) or Geometrical Optics (GO). Either the current-based or ray-based method can quickly approximate the scattered field in the far-field region for SAR imaging. For the first order diffraction, Physical theory of diffraction (PTD) and Geometrical theory of diffraction (GTD) has been implemented to address the diffraction effects. Michaeli's equivalent edge currents (EEC) or other alternative ways to compute the diffraction coefficients along the edges have been derived. Among those methods for far-field radar cross section computation, the current-based ones have been further modified for near field imaging purpose. There are several works on a more accurate evaluation on Green's function for near field PO solution [6, 7, 8]. Also, the modifications of PTD for near field computation were proposed with different ways of calculating near field diffraction coefficients [9].

The most commonly adopted method for multi-bounce scattering is shooting and bouncing ray (SBR) proposed by Hao Ling [10] to solve an open cavity problem. The GO rays represent the incident waves and the paths of each individual ray are determined by Snell's law. They are “shot” into the cavity and bounce back or penetrate through materials. This method can compute the scattered field with cavity for different polarized incident waves and material coating on the wall. In literatures

[11, 12, 13], the SBR has been successfully used to extract scattering center both for 2D and 3D imaging problems. However, the SBR starts to lose the accuracy when the opening is not large enough compared with wavelength, because the field from diffraction effects by the edge on the opening cannot be neglected but now are not taken into consideration.

Other than the ray based method, the Iterative PO (IPO) proposed by Burkholder, R.J. et al in [14] provides a current-based method to take care of both high order reflection and diffraction. This method calculates the high order terms through magnetic field integral equation (MFIE) together with visible rules.

$$\vec{J}(\vec{r}_c) = 2\hat{n} \times \vec{H}_c^i(\vec{r}_c) + \\ 2\hat{n} \times P.V. \int_{S_c} \vec{J}(\vec{r}') \times \hat{R}' \frac{e^{-jkR'}}{4\pi R'} (jk + \frac{1}{R'}) dS' \quad (1.3)$$

where $\vec{R}' = \vec{r}_c - \vec{r}'$, $R' = |\vec{R}'|$, $\hat{R}' = \vec{R}' / R'$, \vec{r}' is an integration point on the surface S_c .

The iterative process used to find \vec{J} for the l^{th} iteration is:

$$\vec{J}^{(l)}(\vec{r}_c) = 2\hat{n} \times \vec{H}_c^i(\vec{r}_c) + \\ 2\hat{n} \times P.V. \int_{S_c} \vec{J}^{(l-1)}(\vec{r}') \times \hat{R}' \frac{e^{-jkR'}}{4\pi R'} (jk + \frac{1}{R'}) dS' \quad (1.4)$$

with the initial solution:

$$\vec{J}^{(0)}(\vec{r}_c) = 2\hat{n} \times \vec{H}_c^i(\vec{r}_c) \quad (1.5)$$

The computation is converged until the difference between the current solution and previous solution is small enough. IPO has been used as the forward solver for near field SAR imaging recently [15]. It provides better solution than SBR, whereas the computation cost is heavy for the SAR imaging due to the complexity of MFIE in each iterative step. The missile example showed in [15] only rotates 30° with 2 GHz bandwidth. When the maximum frequency goes up higher, then the IPO

complexity acts similarly with Moments of Method (MoM), which is undesirable for imaging problem. Instead of simply reduce the complexity of iterative process, Boag [16] combined the IPO together with domain decomposition method to further reduce the complexity with smaller sampling numbers.

For the creeping waves, the high frequency methods such as GO, PO or even the SBR, IPO cannot model the creeping waves. In contrast, the full wave solution from MoM can provide solution of creeping waves yet computationally expensive. In the ray tracing technique, some work have been done to model the creeping rays, where the trajectories can be determined associate with each sampling point on a shadow line, among which the creeping ray is the one that is tangential to the geodesic curve [17]. This method can only approximate the really creeping waves with a dense grid on the shadow line, thus the accuracy highly depends on the number of sampling points on the shadow line.

1.3 Reviews of imaging models

The point scatterer model is the most basic and simplest imaging model suitable for reconstructing the scattering centers corresponding to the single reflection wave phenomenon. The model itself assumes the EM scattered field can be written with a collection of point scatterers, whose amplitude and phase represent the parameters of interest. This model is straightforward and SAR image can be generated through the classic back filtered projection algorithm or 2D IFFT algorithm. However, it is not accurate enough to extract EM parameters from diffraction, multi-bounce and creeping wave mechanisms. First, in high frequency region, the scattering is treated as

quasi-local phenomenon, where the geometrical discontinuous parts of an object contribute most of the scattered field. Consequently, the scattered field is radiated from a finite number of discrete sources at those scattering centers. So, in a more realistic way, the EM scattered field is modeled as a sum of damped sinusoids, and their amplitudes and phases represent the physical parameters. Second, the diffraction effects and creeping wave effects are dependent on the frequency, and this gave the difficulty to inversely extract the scattering center based on the scattered field. The windowing technique is a well known spectrum analysis along with Discrete Fourier Transform (DFT) since we have band limited data. Therefore, a Finite Impulse Response (FIR) filter such as “Hamming” is normally applied together with FFT process. However, in order to identify the scattering centers from different EM mechanisms based on the scattered field, more complicated signal processing models need to be used.

In the following sections, several more sophisticated signal classification methods or algorithms will be introduced for SAR imaging, target feature identification and other EM applications. Generally, polynomial-based signal classification method and model-based signal classification method are two main categories for extracting the scattering centers. And those methods can identify the poles of the system so as to extract the scattering centers and for the image reconstruction process, they are added as Infinite Impulse Response (IIR) filters on top of the Discrete Fourier Transform (DFT).

1.3.1 Prony's method

The first and most classic polynomial-based signal processing method is Prony's Method, which is a quasi-least-squares time-domain IIR filter design method. It was

first invented 1795 by French scientist Baron de Prony. This method is aim to extract the poles of a linear system, which has auto-regressive terms. The details of Pronys method is shown as below [18]:

For a N order causal IIR filter, the transfer function can be written as:

$$H(z) = \frac{\sum_{k=0}^N b_k z^{-k}}{1 + \sum_{m=1}^N a_m z^{-m}} \quad (1.6)$$

That leads to the following relation:

$$H(z) = \sum_{k=0}^N b_k z^{-k} - \sum_{m=1}^N a_m z^{-m} H(z) \quad (1.7)$$

So the output of this system with the above transfer function can be written as:

$$\begin{aligned} h[n] &= \sum_{k=0}^N b_k \delta[n-k] - \sum_{m=1}^N a_m h[n-m] \\ &= \begin{cases} 0 & n < 0 \\ b_n - \sum_{m=1}^N a_m h[n-m] & 0 \leq n \leq N \\ -\sum_{m=1}^N a_m h[n-m] & N < n \end{cases} \end{aligned} \quad (1.8)$$

The original Pronys method matches the impulse response to a desired causal impulse response $d[n]$ at indices $n = 0 \dots 2N$. It is done in two steps:

1. Solve for $a_{m=1}^N$ that yields a match at $n = N+1 \dots 2N$:

$$\underbrace{- \begin{bmatrix} d[N+1] \\ \vdots \\ d[2N] \end{bmatrix}}_{d_{pron}} = \underbrace{\begin{bmatrix} d[N] & d[N-1] & \cdots & d[1] \\ \vdots & \ddots & \ddots & \vdots \\ d[2N-1] & d[2N-2] & \cdots & d[n] \end{bmatrix}}_{D_{pron}} \underbrace{\begin{bmatrix} a[1] \\ \vdots \\ a[N] \end{bmatrix}}_a \Rightarrow a_{pron} = D_{pron}^{-1} d_{pron} \quad (1.9)$$

2. Solve for $b_{n=0}^N$ that yields a match at $n = 0 \dots N$:

$$b[n] = d[n] + \sum_{m=1}^N a_{pron,m} d[n-m] \text{ for } n = 0 \dots N \quad (1.10)$$

The original Prony's method could be inaccurate since we didn't even match the impulse response for $n > 2N$. To elevate this issue, an extended also the most

commonly used Prony's method was proposed, where the approximate match is taken for $d[n]_{n=N+1}^Q$, where $Q > 2N$. A least-squares fit in place of the quality is used for the standard Prony's method (where $Q = 2N$)

$$\begin{aligned}
a_{ext} &= \arg \min_{a_1 \dots a_N} \sum_{n=N+1}^Q \left| (-d[n]) - \sum_{m=1}^N d[n-m]a_m \right|^2 \\
&= \arg \min_a \left\| \underbrace{\begin{bmatrix} d[N] & \cdots & d[1] \\ d[N+1] & \cdots & d[2] \\ \vdots & \ddots & \vdots \\ d[Q-1] & \cdots & d[Q-N] \end{bmatrix}}_{D_{ext}} \begin{bmatrix} a[1] \\ \vdots \\ a[N] \end{bmatrix} - \underbrace{\begin{bmatrix} -d[N+1] \\ -d[N+2] \\ \vdots \\ d[Q] \end{bmatrix}}_{d_{ext}} \right\|^2 \quad (1.11) \\
&= (D_{ext}^H D_{ext})^{-1} D_{ext}^H d_{ext}
\end{aligned}$$

Then we solve for $b_{n=0}^N$ ad we did in standard Prony's method:

$$b_n = d[n] + \sum_{m=1}^N a_{ext,m} d[n-m] \text{ for } n = 0 \dots N \quad (1.12)$$

In summary, this extended Prony's method gives:

$$\begin{aligned}
h[n] &= d[n] \text{ for } n = 0 \dots N \\
h[n] &\approx d[n] \text{ for } n = N+1 \dots Q \quad (1.13)
\end{aligned}$$

and hopefully $h[n] \approx 0 \approx d[n]$ for $n > Q$.

The Prony's method and its variations via Infinite Impulse can be considered as a deterministic nonlinear optimization problem, and these methods are converting the nonlinear minimization of fitting error into the minimization of linear equation error. So the downsides of this method are: first, it only approximates to the true nonlinear optimization problem. Second, it is well known for performing poorly in the presence of noise. Later, the further improvements and alternatives on the polynomial-based methods will be introduced to deal with signals with noise or the true nonlinear optimization problem.

This method has been implemented for the applications of optics, circuit design and electromagnetic. Hurst and Mittra [19] applied this method to the scattering center analysis of 2D and 3D objects and they claimed that with Prony's method, the resolution is improved and the requirement on bandwidth for the spectrum is narrower compared with FFT with "Hamming" window. In addition, this model is rigorous when specular reflection alone is dominant and important, whereas the diffraction can be also appropriately extracted when the dependence on the frequency is slow [19].

1.3.2 Auto-Regressive Moving Average (ARMA) model

ARMA model also wants to get the transfer function (1.6), but it takes one step forward by optimizing the true nonlinear fitting error [20]. The ideal model of the fitting error minimization is:

$$\min_{a,b} \|e\|^2 = \min_{a,b} \sum_{i=0}^{N-1} \left[h_d(i) - \left\{ \frac{N(z)}{D(z)} \right\} \delta(i) \right]^2 \quad (1.14)$$

where $N(z)$ and $D(z)$ are the numerator and denominator of the transfer function; $\frac{N(z)}{D(z)}\delta(i)$ denotes the i^{th} output.

From the literature [21], the numerator (Moving Average) estimation can be modeled as a linear problem whereas the denominator (Auto-Regressive) estimation is a nonlinear problem. Instead of using Prony's method, the nonlinear estimation can be minimized through iterative minimization algorithm. The initial estimate of the ARMA model is derived from the minimization of the linear equation error, which is the solution from Prony's method. From the initial solution, an iterative process is carried out by taking the current l^{th} iteration to update the estimate at $(l+1)^{th}$ iteration until it is finally converged [20]. So the optimization is performed on top of

the minimized equation error solution to achieve the minimized fitting error. Several criterion have been employed for the iterative process, such as Newton method and the prefiltering method [22, 23]. Because of the iterative process, this method has been criticized that the solution is only locally optimized yet not globally optimized [24].

1.3.3 Pencil of functions and Matrix Pencil (MP) Method

The previous two methods and their derivatives are the original “polynomial-based” method, since they need to directly or iteratively solve the coefficients for the polynomial, whose roots provide the poles of the system. They are extremely sensitive in the presence of noise and also not efficient when the number of poles is large. To take the noise into account, the pencil of functions model were used for pole extraction [24, 25]. The noisy signal is represented as:

$$y(k) \equiv x(k) + \sigma W(k) \quad (1.15)$$

where $\sigma W(k)$ is zero mean white noise.

This method starts with a N-order cascaded first order filter, and a set of pencil of functions are created: $y_1 + \gamma y_2, y_2 + \gamma y_3, \dots, y_N + \gamma y_{N+1}$, where y_1, y_2, \dots, y_{N+1} are the inputs for each filter. The key point of this method is to find the values for γ when the set of those pencil of functions is linearly dependent and then the poles of the system can be computed from γ . The details of this method on how to compute the γ based on the correlation matrix can be found in Jain’s paper [24]. It is a variation of the polynomial methods because we are still trying to find the roots of the polynomial through a different way, but the solution is statistically better with noise. Later, with the similar philosophy, a generalized pencil of functions approach:

Matrix Pencil method is proposed [26] to further reduce the computational costs and also overcome the bottlenecks of polynomial methods. Matrix Pencil method is an eigen-structure approach and signal components can be identified exactly by mapping the noise component into the null space. It is one step process in contrast with the two steps process from polynomial methods, and eigenvalues computed are the poles of the system.

The procedure of getting system poles are described in [27]. First, the data matrix is formed from the noisy data:

$$[Y] = \begin{bmatrix} y(0) & y(1) & \dots & y(L) \\ y(1) & y(2) & \dots & y(L+1) \\ \vdots & \vdots & & \vdots \\ y(N-L-1) & y(N-L) & \dots & y(N-1) \end{bmatrix}_{(N-L) \times (L+1)} \quad (1.16)$$

where the L is chosen between $N/3$ to $N/2$ for efficient noise filtering [28]. $[Y_1]$ and $[Y_2]$ are formed by deleting the last column and first column respectively.

The eigen-decomposition is performed on matrix $[Y]$, and the eigenvalues are truncated to keep M dominant ones. Therefore, the matrix $[Y_1]$ and $[Y_2]$ can also be written in a similar way with all the eigenvalues and eigenvectors deriving from $[Y]$. Consequently, the Matrix Pencil is considered as:

$$[Y_2] - \lambda[Y_1] \quad (1.17)$$

and we need to solve for the λ to get all the eigenvalues so as to locate the poles. Equivalently, we can solve the eigenvalues for

$$[Y_1]^+[Y_2] - \lambda[I] \quad (1.18)$$

where the $[Y_1]^+ = [Y_1]^H[Y_1]^{-1}[Y_1]^H$ is the Moore-Penrose pseudoinverse of $[Y_1]$.

The MP method can provide high resolution solution in the presence of noise, but the downsides of this method are 1: the generation of data matrix $[Y]$ requires some prefiltering process to enhance the SNR [29], which are not trivial; 2: the Moore-Penrose pseudoinverse sometimes can be complicated and increases the complexity of this method.

1.3.4 MUTiple SIgnal Classification (MUSIC) algorithm and Estimation of Signal Parameters via Rotational Invariance Technique (ESPRIT)

MUSIC was first developed by Schmidt [30] by deriving a suboptimal solution in the presence of noise. It is one of the most promising methods for many signal processing applications especially the direction-of-arrival (DOA) estimation. This method employs two-step procedure to find the approximate solution. First, an unconstrained set of d vectors through eigendecomposition of the covariance matrix was found to fit the measurement. Then within the signal subspace those d vectors spanned, several points through a closeness approach were sought so as to estimate the parameters.

The data model for signal processing with sensor array is written as:

$$x(t) = A(\theta)s(t) + n(t) \quad (1.19)$$

where $a_k(\theta_i)$ is an element in matrix $A(\theta)$ represents the complex response from a certain sensor, and $n(t)$ is the noise. Then the MUSIC algorithm can be summarized as:

1. Generate the covariance matrix $R_{XX} = AR_{SS}A^* + \sigma^2 \sum_n$
2. Solve the eigensystem $R_{XX}\bar{E} = \sum_n \bar{E}\Lambda$ where $\Lambda = diag\lambda_1, \dots, \lambda_m$ and $\bar{E} = [e_1 | \dots | e_m]$
3. Estimate the number of sources \hat{d}

- Evaluate the closeness through the following formula [30]:

$$P_M(\theta) = \frac{a^*(\theta)a(\theta)}{a^*(\theta)E_N E_N^* a(\theta)} \quad (1.20)$$

where $E_N = \sum_N [e_{d+1} | \cdots | e_m]$.

- Obtain the d (largest) peaks of $P(\theta)$.

MUSIC can provide exact solution when the number of measurements is approaching to infinity. It iteratively searches the nulls of the null spectrum. However, this search over the entire parameter space is expensive especially it goes to multi-dimensional problem. The convergence of the search also could be the local optimum. Later, a variant of MUSIC called root-MUSIC was introduced [31, 32]: a more precise polynomial rooting procedure is used instead of the iterative searching.

ESPRIT is a similar method as MUSIC, which is also based on the eigendecomposition for the covariance matrix, whereas it further decompose the signal subspace into sub matrices [33]. The first 3 steps are exactly the same as MUSIC, the details after that are [34]:

- Decompose the estimate subspace estimate E_s with into E_X and E_Y :
- Compute the decomposition and partition E into $\hat{d} \times \hat{d}$ sub matrices:

$$E_{XY}^* E_{XY} = \begin{bmatrix} E_X^* \\ E_Y^* \end{bmatrix} [E_X | E_Y] = E \Lambda E^* \quad (1.21)$$

$$E \stackrel{\text{def}}{=} \begin{bmatrix} E_{11} & E_{12} \\ E_{21} & E_{22} \end{bmatrix} \quad (1.22)$$

- Compute the eigenvalues of $\Psi = -E_{12} E_{22}^{-1}$ and then estimate the signal parameters.

The essence of the ESPRIT is to find rotation operator Ψ that rotates one set of vectors E_X into another set of vectors E_Y . It is also pointed out in [34] that the decomposition of E_s is not unique for the arrays with multiple invariance. Both MUSIC

and ESPRIT have been implemented with Generalized Singular Value Decomposition (GSVD) instead of eigendecomposition [34, 30].

1.3.5 Other imaging methods

Although the aforementioned methods can identify the magnitudes and phases of the damped sinusoids, the creeping wave scattering mechanism cannot be extracted through those models. The interaction between scattering centers and the amplitude dependence on the frequency make it a challenge for those methods since they assume the amplitudes are independent of frequency[35]. Model-based eigen-decomposition method State Space Model (SSM) is used to address the creeping waves [35]. It is based on the SVD to extract the poles of the system for harmonic retrieval problem [36] and free for all the roots searching for polynomial. The method was further improved by Naishadham [35] for sparse radar signal processing and the application on the radar imaging with creeping waves.

Another group of hot imaging methods recently are time reversal (TR) methods for the indoor imaging such as though-the-wall imaging (TWI). Those TWI are the inverse scattering problems involving in the layer media Green's function, and the objective is to detect whether there are targets inside the wall and their locations. Three main computational TR methods are: TR imaging (TRI) [37, 38], decomposition of reverse time operator (D.O.R.T) [39, 40] and time reversal MUSIC (TR-MUSIC) [41, 42]. The general idea of TR imaging methods is that the array receives the signal and sends out the time reversed wave in time domain or phase conjugated wave in frequency domain to the same probing media. Eventually, the TR waves from different receivers are focused at the target's position. TR-MUSIC is most mature technique to

both improve the imaging quality and efficiency. It is based on the MUSIC method to seek the null space of the response matrix and utilize the null space to provide better resolution in homogeneous media [43].

Chapter 2: Physical Optics with Self-shadowing Technique

2.1 Physical Optics

A scattering problem involving PEC objects can be formulated by Physical Optics [44]. The original problem and the PO approximation can be seen in Figure 2.1, where the fields produced by J_1 and M_1 are E_1 and H_1 . The total field E_{total} and H_{total} can be represented by the summation of incident field and scattered field:

$$E_{total} = E_1 + E_s \quad (2.1)$$

$$H_{total} = H_1 + H_s. \quad (2.2)$$

From the boundary condition, over the boundary S_1 of the conductor, the tangential component of the total electric field vanishes,

$$\hat{n} \times E_{total} = 0, \quad (2.3)$$

which means

$$-\hat{n} \times E_1 = \hat{n} \times E_s, \quad (2.4)$$

and the total tangential component of magnetic field is equal to the equivalent current density J_p ,

$$J_p = \hat{n} \times H_{total} = \hat{n} \times (H_1 + H_s). \quad (2.5)$$

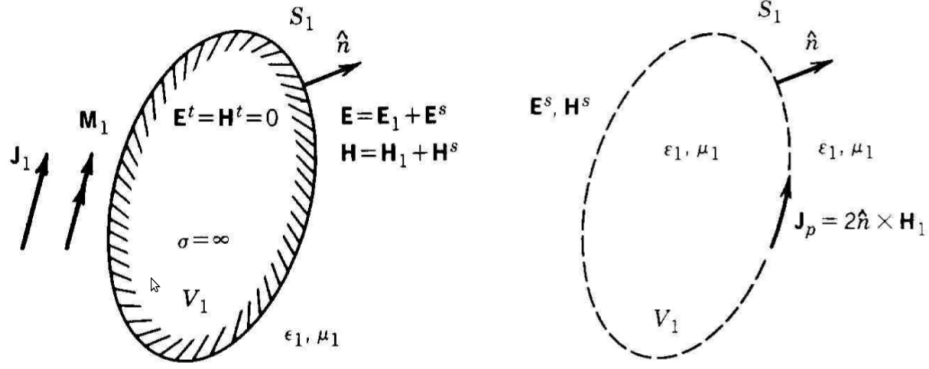


Figure 2.1: (a) Physical equivalent for scattering by a PEC. (b) Approximate physical equivalent for scattering from a PEC.

If the PEC surface is an infinite flat plane, then the tangential components of the scattered field H_s and incident field H_1 are equal. So the electric current J_p is given by

$$J_p = 2\hat{n} \times H_1. \quad (2.6)$$

On the shadow side of an infinite plate, there are no surface currents induced, which leads to

$$J_{po} = \begin{cases} 2n \times H_1, & \text{lit region} \\ 0, & \text{shadow region} \end{cases} \quad (2.7)$$

2.2 Self-shadowing Technique

The PO currents can give good approximation for smooth, electrically large PEC objects at high frequencies. However, in order to maintain the accuracy, the shadow regions of complex scatterers needs to be accurately calculated. Figures 2.2 shows the PO currents with the shadow region computed from (1.1) for a complex target, a ZSU-23-4 at 2 GHz with front-incident excitation. Without considering the object's

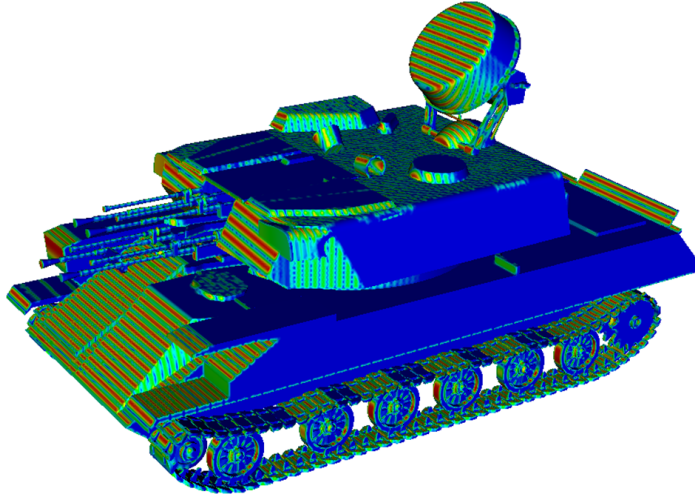


Figure 2.2: Surface currents computed by conventional PO method of ZSU at 2 GHz

self-shadowing, most of the tracks and wheels are mistakenly categorized into the lit region, which provides less reliable results for the scattered field.

The effect of self-shadowing is addressed by using a multi-level Z buffer algorithm. Although it is possible so simply compare each pair of triangles to determine if one shadows the other, this approach would be quadratic in the number of triangles, i.e., $O[(f_{max}R)^4]$, and it would have to be repeated for each aspect angle. This is much too expensive to be practical. Instead, the conventional rule based on (1.1) is first applied to preliminarily compute the lit and shadow regions. Next, the centers of the triangles that are currently in the lit region are projected onto a plane perpendicular to \hat{k}^i . Then the distance between each triangle center and the plane, stored as z depth, represents the physical third dimension of all the triangles projected onto the phase plane. In Figure 2.3, all of the triangles that have been identified as possibly being in the lit region, based on (1.1), have had their centers projected onto a plane, and all have an associated z depth, where smaller z depth indicates being hit by plane

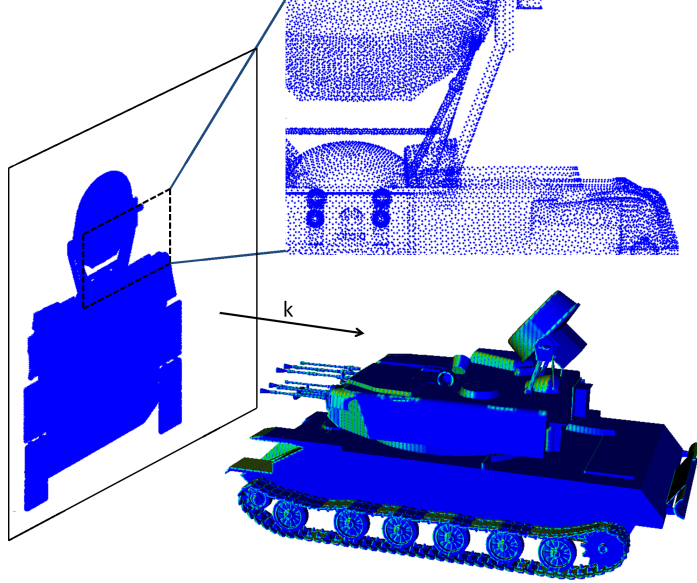


Figure 2.3: Z-buffering projection

wave earlier. If the projected center of any of these triangles lies inside the projection of another lit region triangle and the second triangle's center has a lesser z value, then the first triangle is considered to be shadowed by the second. One way to judge whether a point r_p is inside a convex polygonal surface is to check that

$$[(r_i - r_p) \times (r_{i+1} - r_p)] \cdot \hat{n} > 0 \quad (2.8)$$

for all $i = 1, 2, \dots, M$, where r_i are the consecutively-label vertices of the polyhedron (modulo M). ($r_{N+1} = r_1$) and \hat{n} is the outwards normal direction.

Second, the center points are partitioned using an adaptive quadtree. The root node of the quad tree is initialized to a box containing all the preliminary projection points. Then the root is further divided into four child nodes by bisecting along the X and Y directions. All the child nodes are recursively divided until each partition

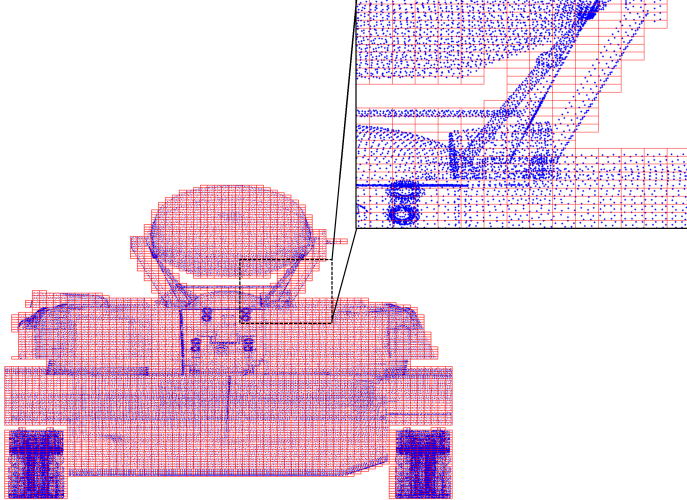


Figure 2.4: Multi-level quad tree partitioning on the projection plane.

contains no more than a given, constant number of points. In this way, assuming a uniform distribution of points, the number of centers that need to be compared for each triangle is bounded. If N is the number of triangles, then at each level of the quadtree there is $O(N)$ work to determine which quadtree box each triangle belongs to. Since there are $O(\log N)$ levels in the final tree, the total work for generating the tree is $O(N \log N) = O[(f_{max}R)^2 \log(f_{max}R)]$.

Next, all the quads in the finest level are looped through to judge the lit region surfaces. Within each quad, the triangles are sorted by z depth, so that we can go through the triangles from least to greatest distance, since surfaces that occur earlier along the incident field direction are more likely to block other surfaces. The triangles that could potentially be blocked by a given lit triangle are only those that are in the lit triangles quad or the neighboring quads, as shown in Figures 2.5. Under the assumption that the mesh triangles are uniformly distributed, then each quad has

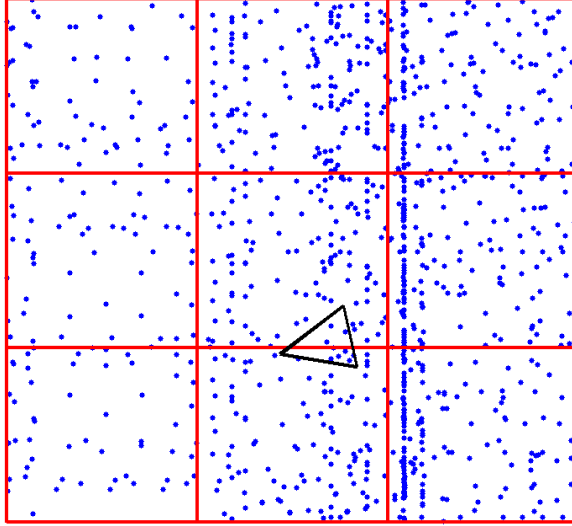


Figure 2.5: Identification of hidden surfaces for one triangle

$O(1)$ triangles to check and also $O(1)$ potential blockers in itself and the neighboring quads. Therefore, the time to find the lit and shadowed triangles in each quad is bounded by a constant, and the total complexity is $O(N)$. However, the time to find the neighboring quads should also be considered. Because the quads are uniformly refined, the depth of the quad tree, and thus the cost of a binary search, is $O(\log N)$. This must be done for each quad, in order to find its neighbors, making the total search time $O(N \log N)$. Therefore, the total complexity for this self-shadowing algorithm is $O(N \log N)$. However, practically the complexity is smaller than $O(N \log N)$ since the computation is dominated by the comparing the triangles for shadowing, which is $O(N)$. When applying the self-shadowing algorithm, in Figures 2.2 the parts that are block by the object itself have been removed, compared with the original calculation in Figures 2.6.

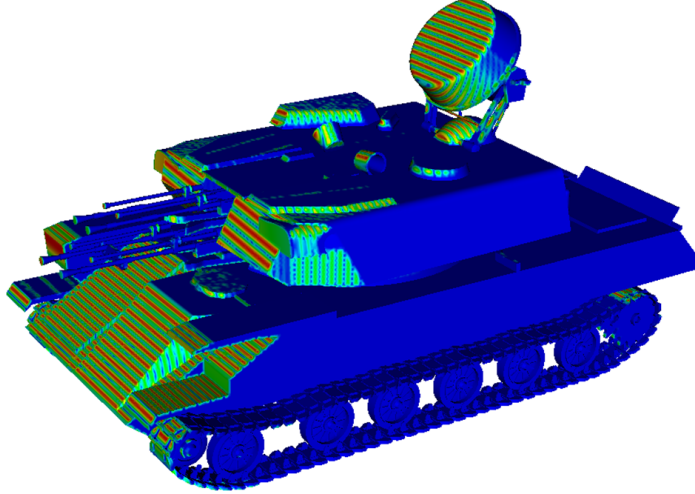


Figure 2.6: Surface currents computed by the improved PO method of ZSU at 2 GHz

Table 2.1: Computation time on lit region identification with Z-buffer algorithm.

Number of facets	Frequency	Computation Time
685,000	4 GHz	1.03 s
2,740,144	8 GHz	4.35 s
10,960,576	16 GHz	18.55 s

Eventually, with this optimized z-buffering algorithm, we solve the ZSU model at 4 GHz, 8 GHz and 16 GHz, with the total number of triangles proportional to $(kd)^2$. The computation time spent on identifying the real lit and shadow region increases approximately linearly, as seen in Table 5.1. All simulations were performed using OpenMP parallelization on a dual-socket computer using Intel Xeon X5450 processors, for a total of eight 3.0 GHz cores. The computation time is plotted with different frequencies in Figures 2.7, where we can see the computation time fits better for the

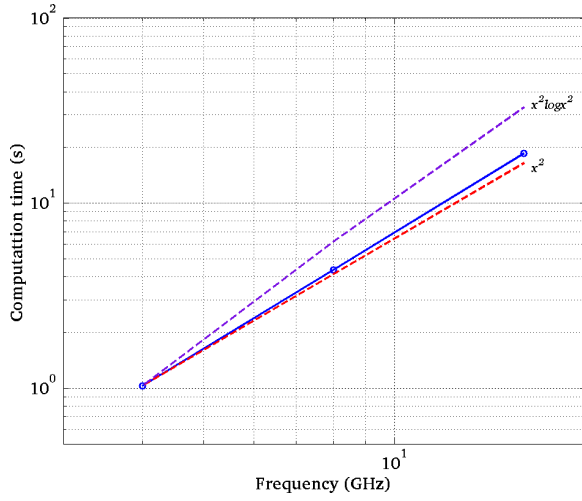


Figure 2.7: Computation time of self-shadowing algorithm for ZSU-23-4 at different frequencies.

x^2 curve which is the $O(N)$ complexity. That is because in the worst scenario, the complexity is $O(N) + O(N \log(N))$, where N is the total number of triangles, but in practice the self-shadowing algorithm is only performed on the lit pre-computed region triangles, which are a subset of the total triangles. Additionally, the bi-static VV and HH scattered field of the tank at 2 GHz is also simulated using the self-shadowing algorithm, as seen in Figures 2.8, resulting in better agreement with the full wave solution.

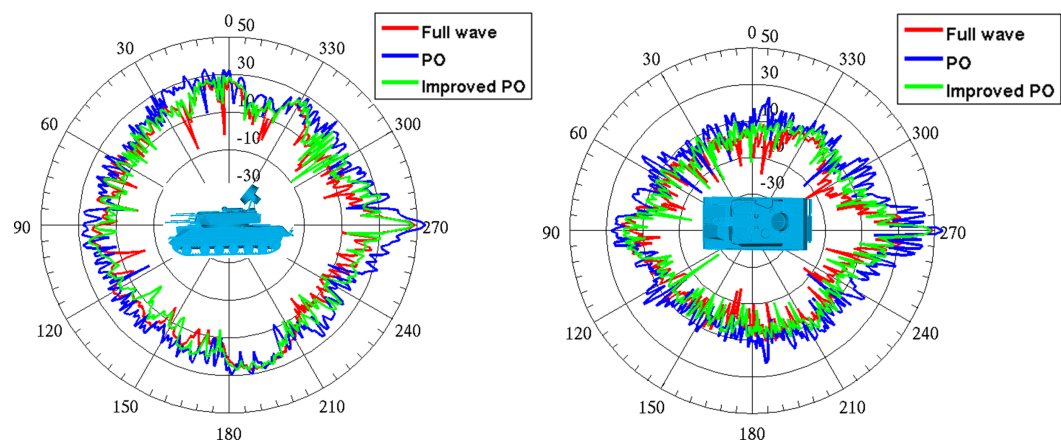


Figure 2.8: (a)Comparison of VV scattered fields of the ZSU at 2 GHz with 30° elevation angle. (b)Comparison of HH scattered fields of the ZSU at 2 GHz with 30° elevation angle.

Chapter 3: Farfield Integration for Physical Optics

3.1 Far-field integral with PO approximation

With the self-shadowing algorithm introduced from the previous chapter, the PO currents are computed in a more accurate lit region, and then we are focused on the next step: the evaluation of PO far-field integral. Generally, to obtain the far-field components of the scattered field, there are a few approximations to the Green function are used:

$$\begin{aligned} G(r, r') &= \frac{e^{-jk|r-r'|}}{4\pi|r-r'|} \approx \frac{e^{-jk_0r}}{4\pi r} e^{+jk_0\hat{r}\cdot r'} \\ \nabla \times G(r, r') \vec{A} &\approx -jk_0 \frac{e^{-jk_0r}}{4\pi r} (\hat{r} \times \vec{A}) e^{jk_0r'} \\ \nabla \times \nabla \times G(r, r') \vec{A} &\approx (-jk_0)^2 \frac{e^{-jk_0r}}{4\pi r} (\hat{r} \times \hat{r} \times \vec{A}) e^{jk_0r'} \end{aligned} \quad (3.1)$$

Plugging in the above approximations, the far-field representation formula from equivalent surface currents $\vec{J}_s(\vec{r}')$ and $\vec{M}_s(\vec{r}')$ becomes:

$$\begin{aligned} \vec{E}_s(r) &\approx j\omega\mu_0 \frac{e^{-jk_0r}}{4\pi r} \cdot \hat{r} \\ &\times \int_{s'} \left[\hat{r} \times \vec{J}_s + \frac{1}{Z_0} \vec{M}_s \right] e^{+jk_0r'} dr'. \end{aligned} \quad (3.2)$$

The above representation formula is a general far field integration expression for any equivalent electric and magnetic surface currents. In the PO approximation for

PEC objects, the equivalent magnetic currents $\vec{M}_s(\vec{r})$ is equal to zero, so the far-field integral (3.2) is simplified into (3.3) by substituting the PO currents: $\vec{J}_s(\vec{r}) = 2\hat{n} \times \vec{H}_{inc}$ in the lit region.

$$\begin{aligned}\vec{E}_s(r) &= \frac{jkE_0 \exp(-jk_0 r)}{2\pi r} \hat{r} \\ &\times \int_{S_1} \hat{r} \times (\hat{n} \times \vec{H}_{inc}) e^{-jk_0(\hat{i}-\hat{r}) \cdot r'} dr',\end{aligned}\tag{3.3}$$

where \hat{n} is the normal direction of the surface, \hat{i} is the unit vector in the incident wave direction, and \hat{r} is the unit vector in the scattered field direction.

One classical way to numerically evaluate this integral is to use Gaussian quadrature rules, which takes the weighted summation of function values at the quadrature points on the surface. However, the accuracy depends on the number of quadrature points, and the element size needs to meet Nyquist sampling rules. With Gaussian quadrature rules, the scattered can be evaluated with N Gaussian points in the following forms:

$$\begin{aligned}\vec{E}_s(\vec{r}) &= \frac{jkE_0 \exp(-jk_0 r)}{2\pi r} \hat{r} \\ &\times \sum_{i=1}^N w_i \hat{r} \times (\hat{n} \times \vec{H}_{inc}) e^{-jk_0(\hat{i}-\hat{r}) \cdot r'_i},\end{aligned}\tag{3.4}$$

where w_i is the weighted function for i th Gaussian points on the surface and its location is r'_i .

3.2 Gordon's method

Asides Gaussian quadrature integration, other methods that applied to evaluate PO far-field integral were presented in the literatures [5, 45, 46]. Among those methods, Gordon's method can convert the double integral into simpler single integral for the flat surfaces, which provide an analytical solution independent of frequency [5].

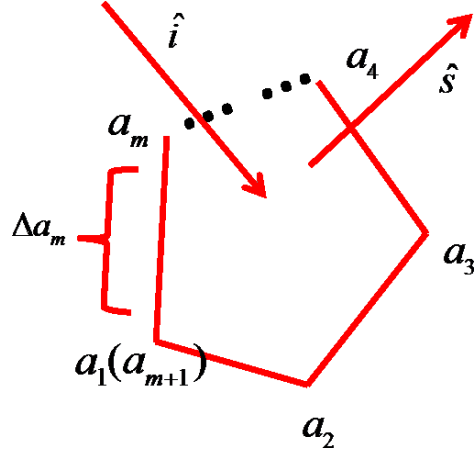


Figure 3.1: Surface currents computed by the improved PO method of ZSU at 2 GHz

First, on an arbitrary flat surface, the evaluation of scattered field at r direction with incident wave coming from i direction is given by:

$$\begin{aligned}
 \iint_S e^{ik\hat{\delta} \cdot x} dx_1 dx_2 &= \frac{\hat{i}}{k(|\hat{\delta}|^2 - (\hat{\delta} \cdot \hat{n}_n))^2} \int_{\partial S} e^{ik\hat{\delta} \cdot x} (\delta_2 dx_1 - \delta_1 dx_2) \\
 &= \frac{\hat{i}}{k(|\hat{\delta}|^2 - (\hat{\delta} \cdot \hat{n}_n))^2} \int_{\partial S} e^{ik\hat{\delta} \cdot x(t)} (\hat{\delta}^* \cdot x(t)) \\
 &= \frac{\hat{i}}{k(|\hat{\delta}|^2 - (\hat{\delta} \cdot \hat{n}_n))^2} (T_1 + T_2 + \dots + T_N)
 \end{aligned} \tag{3.5}$$

where $\hat{\delta} = \hat{s} - \hat{i}$, $\hat{\delta}^* = \hat{\delta} \times \hat{n}_n$, $x(t) = (1-t)a_n + ta_{n+1}$

If the surface is an N-gon as shown in Figures 3.1, then the integration becomes the summation of N terms, where T_n is described in equation 3.6. The proof of this expansion from double integral to single integral can be found in Appendix I by using Stoke's theorem.

$$T_n = (\hat{\delta}^* \cdot \Delta a_n) \text{sinc}\left(\frac{k}{2}\hat{\delta} \cdot \Delta a_n\right) e^{\frac{ik}{2}\hat{\delta} \cdot (a_n + a_{n+1})} \tag{3.6}$$

With the application for SAR imaging, we are only interested in the backward direction. So the mono-static scattered field contributing from a surface $\Delta_i \subset \Gamma_{h,lit}$ is proportional to the oscillatory kernel:

$$\int_{\Delta_i} \exp(2jk\hat{k}^i \cdot \vec{r}') d\vec{r}'. \quad (3.7)$$

With Gordon's method, the mono-static scattered field from a flat surface can be written with the following form, where \vec{a}_n represents the position vector of the n^{th} vertex of the polygon.

$$\begin{aligned} \vec{E}_s(\vec{r}) = & -E_{inc} \frac{e^{-jk_0 r}}{r} \frac{\hat{r} \times \hat{r} \times (\hat{n}_n \times \vec{H}_{inc})}{2\pi [(|\hat{r} - \hat{i}|^2 - ((\hat{r} - \hat{i}) \cdot \hat{n}_n))^2]} \\ & \sum_{n=1}^M [((\hat{r} - \hat{i}) \times \hat{n}_n) \cdot \Delta \vec{a}_n] \operatorname{sinc}\left(\frac{k}{2}(\hat{r} - \hat{i}) \cdot \Delta \vec{a}_n\right) \\ & \exp\left(\frac{jk}{2}(\hat{r} - \hat{i}) \cdot (\vec{a}_n + \vec{a}_{n+1})\right) \end{aligned} \quad (3.8)$$

With the Gordon's method for mono-static scattered, we compute the scattered field by integrating all over the lit region triangles of ZSU-23-4 at 2 GHz with front-incident 30° elevation angle plane wave. The computation time from both Gaussian quadrature rules and Gordon's method are compared in Table 3.1. The number of operators of Gordon's method is much less than the surface integral's number of operators, but if the number of elements are meshed with respect of frequency the computation time is still proportional to f^2 . It is faster to use Gordon's method and this offers a tantalizing possibility: if Γ is composed largely of planer regions, then Gordon's method can be used to make the number of triangles almost independent of frequency.

For the mesh of curved surfaces to remain smooth on scales comparable to λ , however, the number of triangles must remain frequency-dependent. So in this work,

N	f (GHz)	time (quadrature)	time (Gordon)
685,000	4	2.45 s	0.35 s
2,740,144	8	9.75 s	1.31 s
10,960,576	16	39.13 s	5.26 s

Table 3.1: Far-field evaluation time for ZSU-23-4

the object is adaptively mesh to capture the geometrical accuracy, where the curved surfaces are meshed much finer than the large flat surfaces. Then another issue shows up that if only one mesh has been used throughout the whole frequency range sweep, the accuracy of self-shadowing techniques is jeopardized since the number of element per wavelength is not sufficient. So the trade off is made between accuracy and complexity that we use same adaptive mesh generated at middle frequency of the desired frequency range.

Even with the current integration, the complexity of computing the full spectrum is still undesirable. Without any acceleration technique, we need to integrate over all the lit region triangles at each (f, θ) point. And this gives a complexity of $O((k_{max}R)^4)$ if the mesh size is proportional to wavelength. So the further improvements regarding reducing the total sampling points for direct integrations are introduced in the next few sections.

3.3 Accelerated Frequency Sampling

In order to get 2-D spectrum, the calculation of the scattering pattern can be further accelerated by decomposing the whole object into smaller domains since smaller

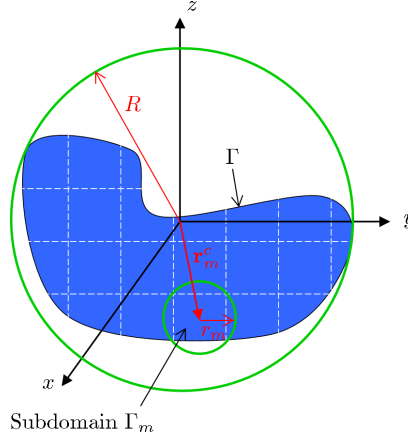


Figure 3.2: Scattering pattern from smaller domains

objects require fewer frequency samples [47]. Consider the perfectly electrically conducting (PEC) object in Fig. 3.2.

The original object is contained in a large sphere of radius R . If we divide surface into partitions $\Gamma_1, \dots, \Gamma_M$ and now the one of the smaller domains is bounded by r . Then the mono-static field can be expanded by the following expression:

$$\sigma(k, \phi, \Gamma, \vec{0}) = \int_{\Gamma} A(\theta, \phi, \vec{r}') e^{-2jk\vec{k} \cdot \vec{r}'} d\vec{r}', \quad (3.9)$$

where $A(\theta, \phi, \vec{r}') = (\hat{n} \cdot \hat{r}) \ell(\theta, \phi, \vec{r}')$ and ℓ is the lit region function, equal to one if \vec{r}' is visible from the direction (θ, ϕ) and zero otherwise. It was pointed out in [47] that to interpolate this function versus frequency, the sampling interval should satisfy $\Delta f < c/4R$. This can be intuitively understood as follows: the PO approximation physically corresponds to simulating a single reflection of the incident field off of the scatterer. In the time domain, one need not observe the reflected wave for a longer period of time than $4R/c$ to see all of the single-reflection effects. However, a basic result in sampling theory says that if a signal is observed for time T , its spectrum

cannot be determined with a resolution greater than $\Delta f = 1/T$. Because the single-reflection effects modeled by PO only contribute to the first $4R/c$ of the reflected signal, a frequency interval of $c/4R$ is sufficient to recover the spectrum.

Now, suppose that the lit region has been divided into M partitions $\Gamma_1, \dots, \Gamma_M$, each of which has a minimum bounding sphere with radius r_m , centered at \vec{r}_m^c . Then (3.9) can be rewritten as

$$\begin{aligned}
\sigma(k, \phi, \Gamma, \vec{0}) &= \sum_{m=1}^M \sigma(k, \phi, \Gamma_m, \vec{0}) \\
&= \sum_{m=1}^M \int_{\Gamma_m} A(\theta, \phi, \vec{r}') e^{-2jk\hat{k}\cdot(\vec{r}' - \vec{r}_m^c)} e^{-2jk\hat{k}\cdot\vec{r}_m^c} d\vec{r}' \\
&= \underbrace{\sum_{m=1}^M e^{-2jk\hat{k}\cdot\vec{r}_m^c}}_{\text{phase factor}} \underbrace{\int_{\Gamma_m} A(\theta, \phi, \vec{r}') e^{-2jk\hat{k}\cdot(\vec{r}' - \vec{r}_m^c)} d\vec{r}'}_{\text{partition far field}} \\
&= \sum_{m=1}^M e^{-2jk\hat{k}\cdot\vec{r}_m^c} \sigma(k, \phi, \Gamma_m, \vec{r}_m^c)
\end{aligned} \tag{3.10}$$

It can be seen that the total scattered field is composed of a number of signals, each of which consists of the partition far field modulated by a rapidly oscillating phase factor. Since the partition far fields have lower bandwidth, significant savings can be achieved by sampling it with a larger interval, proportional to $4r_m/c$, and interpolating to the finer sampling rate needed by the entire scatterer.

To be concrete, we suppose that, given an incident wave direction (θ, ϕ) , it is desired to calculate the scattered over the frequency range $[f_{min}, f_{max}]$. The scattered field of the entire scatterer is calculated at $N_f = C_f(f_{max} - f_{min})4R/c$ equally-spaced frequencies, where C_f is an oversampling factor greater than or equal to one. Likewise, the m -th partition has $\bar{N}_f^q = C_f(f_{max} - f_{min})4r_m/c$ frequency samples. These can be

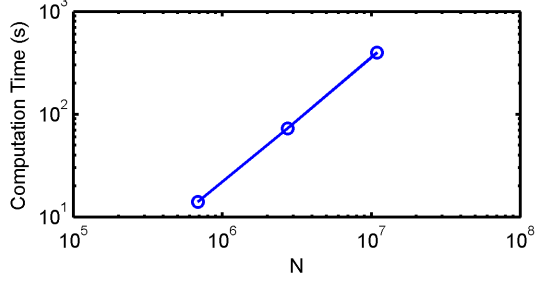


Figure 3.3: Comparison between the interpolated and direct computed scattered field for ZSU-23-4 at 2 GHz.

arranged into a vector

$$\vec{u}_i^m = \sigma(\bar{k}_i, \phi, \Gamma_m, \vec{r}_m^c). \quad (3.11)$$

Then, the scattered field from the entire object can be approximated as

$$\vec{u}_i \approx \sum_{m=1}^M \exp(-2jk_i \hat{r} \cdot \vec{r}_m^c) I_{N_f, \bar{N}_f^q} \vec{u}_i^m, \quad (3.12)$$

where $I_{X,Y}$ is an operator that interpolates from Y samples to X .

Because $d_i = \sup_{\vec{r} \in \Gamma_i} \|\vec{r} - \vec{r}_i^c\| < \sup_{\vec{r} \in \Gamma_i} \|\vec{r}\|$, the right-hand side integral has a smaller bandwidth. Therefore, for each partition, we can calculate the lower-bandwidth integral at $O(f_{max}d_i)$ samples, use interpolation to up-sample to $O(f_{max}R)$, multiply by the phase factor, and add the result to that of the other partitions. The cost to combine partitions' σ samples is $O(Mk_{max}R)$. So the total cost is $Nk_{max}r + Mk_{max}R = N\sqrt{N/M} + M\sqrt{N}$. It can be shown that the choice $M = O(N^{2/3})$ results in complexity $O(N^{7/6}) = O[(f_{max}R)^{7/3}]$ for a single aspect angle.

To validate this frequency acceleration technique, we first simulate the frequency sweep from 12 MHz to 3 GHz for a sphere with 1 meter radius. The whole sphere is meshed with 2970 triangles and partitioned into 140 groups. The second example is the frequency sweep from 12 MHz to 2 GHz for a $1 \text{ m} \times 1 \text{ m} \times 1 \text{ m}$ cube with

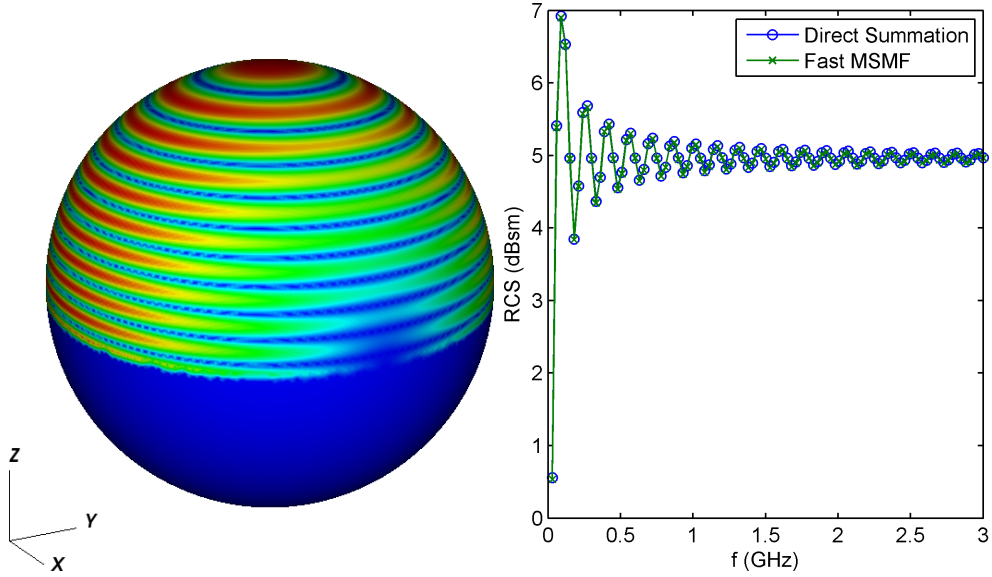


Figure 3.4: Fast frequency acceleration for 1 meter sphere from 12 MHz to 3 GHz with top incident plane wave.

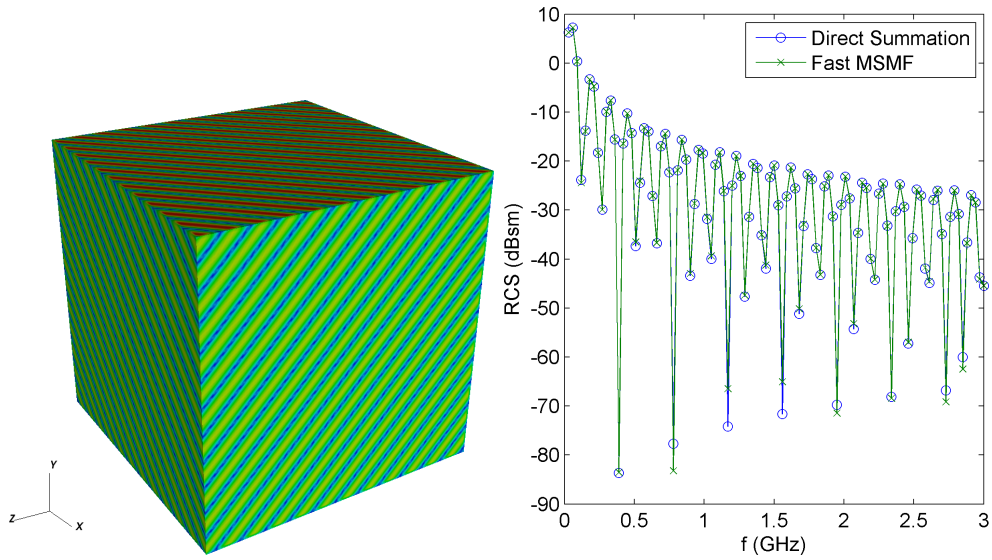


Figure 3.5: Fast frequency acceleration for 1m*1m*1m cube from 12 MHz to 3 GHz with $\theta = 45^\circ$, $\phi = 45^\circ$ incident plane wave.

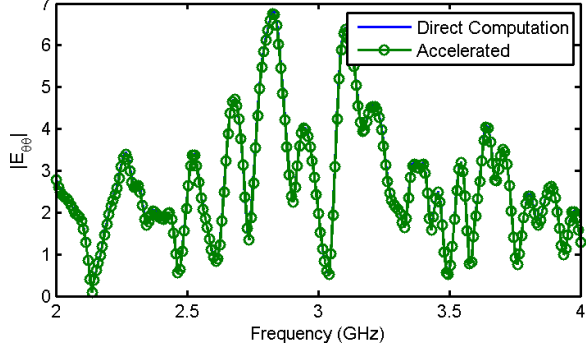


Figure 3.6: Comparison between the interpolated and direct computed scattered field for ZSU-23-4 at 2 GHz.

$\theta = 45^\circ$, $\phi = 45^\circ$ incident plane wave. The whole cube is meshed with 888 triangles and partitioned into 100 groups. Figures 3.4 and 3.5 show the scattered field from direct computation and interpolation, where a good agreement is achieved.

The last example we compute the mono-static field for ZSU-23-4 from 2 GHz to 4 GHz with 30° elevation angle. The total number of triangles in the mesh is 1,040,686 partitioned into 980 groups and receives total computation time 2.45 s. From Figures 3.6 we can see a good agreement between direct computation and interpolation.

3.4 Multi-Frequency Multi-Angle Acceleration

The previous technique shows how to reduce frequency samples, then the question is how to also reduce the angular samples. Although the angular sampling can be accelerated in the same way, it is slightly more complicated than [47] due to self-shadowing.

Since the lit region function is $\ell(\theta, \phi, \vec{r})$ is function of incident angle, we need to assume the lit region function $\ell(\theta, \phi, \vec{r})$ has a small bandwidth and also can be

interpolated. By using a similar concept, instead of interpolating the scattered field in frequency domain, the spectrum is computed both in frequency and angular domain within each smaller group. Then a linear 2D interpolation is used to interpolation the contribution from each smaller group to the whole object. The integrand with respect to frequency f is proportional to $(f_{max} - f_{min})4r_m/c$. And similarly the integrand with respect to angle (θ, ϕ) is proportional to $f_{max}4r_m/c$ for every one radian. In this case the range of angular sweep is $[0, 2\pi]$ for the entire object, then within each group the integrand bandwidth is proportional to $f_{max}8\pi r_m/c$. So the expansion for 2D accelerated scattered field computation is the same with (3.10), but the difference is $\ell(\theta, \phi, \vec{r})$ is changing with incident direction (θ, ϕ) and the number of sampling points is the different in angular domain.

If the desired scattered field lies in the frequency range $[f_{min}, f_{max}]$ and angular range $[0, 2\pi]$, then the scattered field of the entire scatterer is calculated at $N_f \times N_a$ equally-spaced points in frequency-angular domain, where $N_f = C_f(f_{max} - f_{min})4R/c$ and $N_a = C_a f_{max}8\pi R/c$. C_f and C_a are oversampling factor greater than or equal than one. So the m -th partition has $N_f^q \times N_a^q$ samples, where $N_f = C_f(f_{max} - f_{min})4r_m/c$ and $N_a = C_a f_{max}8\pi r_m/c$. These can be arranged into a new vector

$$\vec{u}_{ij}^m = \sigma(\bar{k}_i, \phi_j, \Gamma_m, \vec{r}_m^c). \quad (3.13)$$

Then, the scattered field from the entire object can be approximated as

$$\vec{u}_{ij} \approx \sum_{m=1}^M \exp(-2jk_i \hat{r} \cdot \vec{r}_m^c) I_{N_f, \bar{N}_f^q, N_a, \bar{N}_a^q} \vec{u}_{ij}^m, \quad (3.14)$$

where $I_{X1, Y1; X2, Y2}$ is an operator that interpolates from $Y1 \times Y2$ samples to $X1 \times X2$ samples.

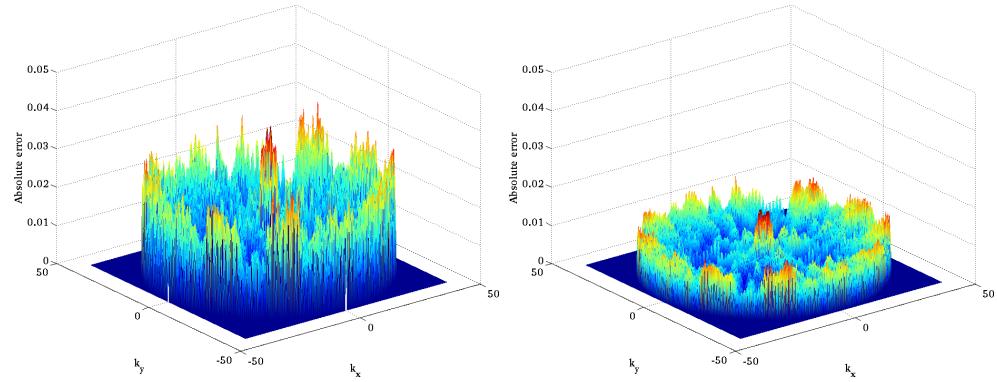


Figure 3.7: Multi-frequency multi-angle acceleration for sphere from 12 MHz to 2 GHz. (a) Absolute error with $C_f = 2.0$, $C_a = 2.0$. (b) Absolute error with $C_f = 3.0$, $C_a = 3.0$

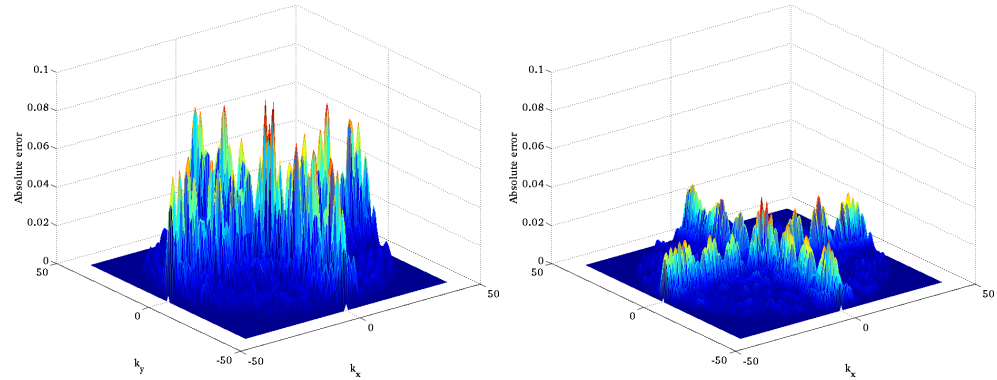


Figure 3.8: Multi-frequency multi-angle acceleration for cube from 12 MHz to 2 GHz (a) Absolute error with $C_f = 2.0$, $C_a = 2.0$. (b) Absolute error with $C_f = 3.0$, $C_a = 3.0$.

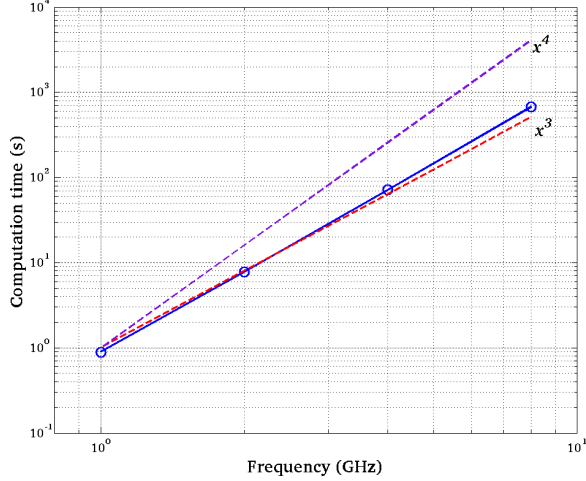


Figure 3.9: Computation time for a sphere with different maximum frequencies.

Figures 3.7 and 3.8 display the scattered field from direct computation and interpolation for a 1 meter radius sphere and a $1\text{ m} \times 1\text{ m} \times 1\text{ m}$ cube. The computation for the sphere is from 10 MHz to 2 GHz with 0° elevation angle and we achieve Root Mean Square (RMS) error: 1.57% when the oversampling factor $C_f = 2.0$ and $C_a = 2.0$. When both of the oversampling factors increase from 2.0 to 3.0, the RMS error goes down to 0.69%. On the other hand, the cube is computed from 10 MHz to 2 GHz with $\theta = 45^\circ$, $\phi = 45^\circ$, and the RMS error here is 6.23% when the oversampling rate factors are both 2.0. The RMS error drops to 2.45% when they are both 3.0. From this study, we can conclude this method is error controllable, because if the sampling number inside each partition increases, the interpolation solution becomes more accurate. For the future examples, the computation is finished with oversampling factor $C_f = 2.0$ and $C_a = 1.0$ to achieve the compromise between the accuracy and complexity.

For this 2D acceleration algorithm, the total cost for the direct computation for the scattered field from each partition is $N(kr)^2$, where r is the bounding radius for the partition. For both frequencies and angles sampling, the complexity is $O(kr)$. Next step is to interpolate the full 2D scattering pattern from each local scattering pattern. For each partition, interpolate from $O(kd)^2$ sampling grid to $O(kr)^2$ grid costs $M(kR)^2$. To add together partition far fields to obtain global far field, the computation cost is $M(kR)^2$. Thus, the total cost for 2D acceleration algorithm is: $O\left(N(kr)^2 + M(kR)^2\right) = O(N^2/M + NM)$. In order to achieve the optimal complexity, the number of partitions is chosen as $M = O(\sqrt{N})$ so eventually the minimized complexity is $O(N^{3/2})$. An example to show the actual complexity is the 1 meter radius sphere, which is simulated with maximum frequency as 1 GHz, 2 GHz, 4 GHz and 8 GHz respectively. The original sphere for 1 GHz computation is meshed into 2970 triangles, then it is refined 4 times as the frequency doubles. So basically, the total number of triangles are proportional to $(kR)^2$, then theoretically the total complexity to get the full spectrum is $O(kR)^3$. From Figure 3.9 we can see the real computation time curve for a sphere with different maximum frequencies matches the k^3 curve very well. But in this work, we choose the same mesh to simulate the whole tank, where the maximum element size is $\lambda/3$ to $\lambda/4$ corresponding to frequency at 5 GHz. With this adaptive mesh, the number of triangles and partitions won't be scaled with frequency, so the complexity to simulate the tank can be further reduced to $O(kR)^2$.

In summary, with the multi-frequency multi-angle acceleration algorithm, we compute the 2D spectrum for the entire object at a lower sampling rate compared with Nyquist sampling rate by dividing the object into smaller groups. The reason this

method is valid is because we use a narrow band signal modulated by a high frequency “carrier”, so the sampling rate has been decreased due to the lower bandwidth of signal, which is corresponding to the scattered field from the smaller domains.

Chapter 4: Synthetic Aperture Radar Imaging

4.1 Introduction to SAR Imaging

A simple and widely used model for ISAR imaging is to assume that the target consists of a large number of point scatters [48]. The goal is then to determine the range and distribution of these scatters, thereby forming an image of the target. Let's first look at one-dimensional imaging scenario in Figure 4.1.

The range and reflectivity values of these targets, marked as (x_n, σ_n) , are the unknowns we are trying to retrieve. A transmitting/receiving radar is located at the same cross-range location, and the range x_n and reflectivity σ_n of the targets can be

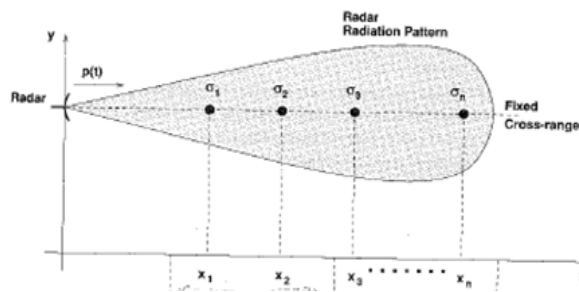


Figure 4.1: Illustration of down range imaging.

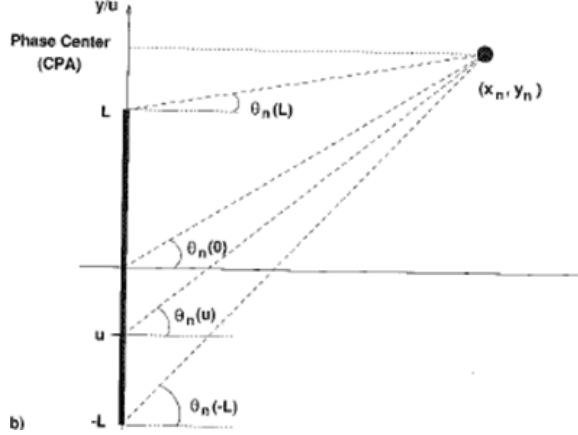


Figure 4.2: Illustration of cross range imaging.

identified through the ideal down range function

$$f_0(x) = \sum_n \sigma_n \delta(x - x_n). \quad (4.1)$$

Similar to the down range imaging problem, Figures 4.2 shows cross range imaging system, for which the ideal target function in the cross-range domain is:

$$f_0(y) = \sum_n \sigma_n \delta(y - y_n) \quad (4.2)$$

So if we illuminate a one-dimensional target area with a wave $p(t)$, for instance, in the x domain, then the received echo signal has the form:

$$s(t) = \sum_n \sigma_n p\left(t - \frac{2x_n}{c}\right), \quad (4.3)$$

where $\frac{2x_n}{c}$ is the time delay for the radar signal to travel from the radar to the n -th target and back to the radar.

If the radar transmits a continuous wave signal, then $p(t) = \exp(j\omega t)$. The recorded of n -th radar from the target located at (x_n, y_n) is

$$\begin{aligned} s(t, u) &= \sum_n \sigma_n p \left[t - \frac{2\sqrt{x_n^2 + (y_n - u)^2}}{c} \right] \\ &= \exp(j\omega t) \sum_n \sigma_n \exp \left[-j2k\sqrt{x_n^2 + (y_n - u)^2} \right] \end{aligned} \quad (4.4)$$

After fast-time baseband conversion, the recorded signal becomes

$$s(\omega, u) = s(t, u) \exp(-j\omega t) = \sum_n \sigma_n \exp[-j2k\sqrt{x_n^2 + (y_n - u)^2}] \quad (4.5)$$

In order to reconstruct the image with all the recorded signals from radar receiver, two reconstruction methods are most commonly used in the literature: direct Fourier reconstruction and back-filtered reconstruction. The 2-D direct reconstruction algorithm performs the discrete Fourier transform in the (ω_x, ω_y) domain, where the FFT can be employed to reduce the complexity. However, the accuracy of this method depends highly on the interpolation from a polar grid to a Cartesian grid, and the whole imaging process cannot start until all the data are gathered. In contrast, the standard back projection algorithm allows the data to be “pipelined”, to reconstruct the image angle by angle. But this algorithm suffers huge computational cost. Regardless of the memory usage, the trade off between complexity and flexibility favors the direct 2-D Fourier transform method, because it is the most straightforward way to get the image and $N \log N$ complexity can be achieved by the fast Fourier transform.

In this work, the actual SAR imaging system we set up is based upon the circular synthetic aperture radar method described by Soumekh [2]. It requires that the radar illuminate the entire target from many different angles, particularly we use full rotation range where $\phi = [0, 2\pi]$. Figures 4.3 shows a typical 2D SAR imaging system with an aircraft carrying transmitter and receiver, and this image shows the

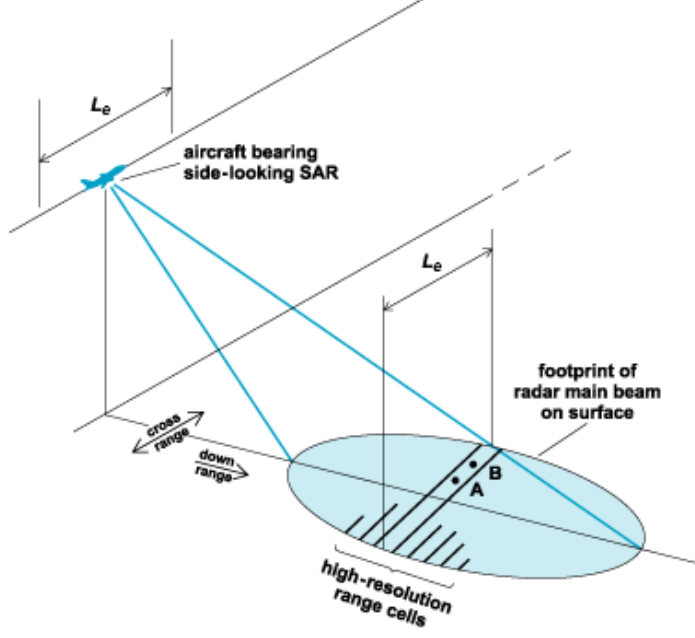


Figure 4.3: Illustration of 2D SAR imaging system.

side-looking SAR image so the aircraft flies long a straight line. The model we use here is assuming the aircraft is flying around the target area for a full circle. The antennas carrying by the aircraft receive the echo from a certain elevation angle θ_z . All the echo information is simulated through PO solution in the frequency domain.

The spectrum is first simulated in the $k - \theta$ domain then converted into the $k_x - k_y$ domain as shown in Figures 4.4.

$$F[k_x(\rho, \theta), k_y(\rho, \theta)] = F_p(\rho, \theta), \quad (4.6)$$

where

$$k_x(\omega, \phi) = (\omega/c) \cos(\phi) \quad (4.7)$$

$$k_y(\omega, \phi) = (\omega/c) \sin(\phi) \quad (4.8)$$

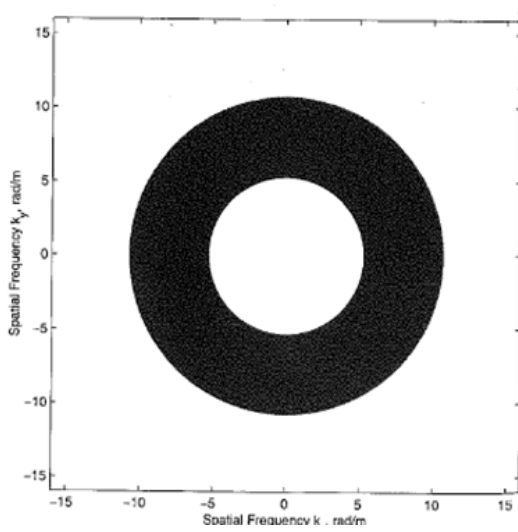


Figure 4.4: 2D spectrum for SAR imaging in $k_x - k_y$ domain.

From the back-scattered field, a full 2-D IFFT is performed on the spectrum in Cartesian grid to get the spatial function $O(x, y)$, which can be described as:

$$O(x, y) = \int F(k_x, k_y) \exp [j(k_x x + k_y y)] dk_x dk_y. \quad (4.9)$$

From the Fourier transform, we know that the resolution in spatial domain is determined by the maximum frequency. The polar samples are within the spatial frequency band:

$$\sqrt{k_x^2 + k_y^2} \leq 2k_{max} \cos(\theta_z) \quad (4.10)$$

Then after the inverse DFT of the target spectrum, the spatial resolution of the reconstructed image is:

$$\Delta y = \Delta x = \frac{\pi}{2k_{max} \cos(\theta_z)} \quad (4.11)$$

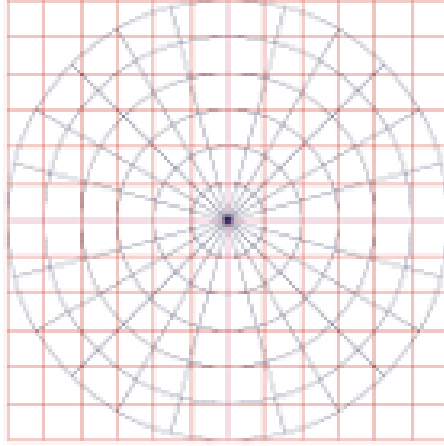


Figure 4.5: Illustration of interpolation from Polar to Cartesian grid data.

4.2 Polar to Cartesian Grid Interpolation

From the previous section, we know the spectrum directly computed from numerical methods is evenly-spaced in polar grid. However, the spectrum in the (k_x, k_y) domain needs to be evenly-spaced if the uniform FFT is to be used to generate the image, so the interpolation from the polar (k, ϕ) grid to the Cartesian grid is important [49, 50]. Among the prior work on the SAR imaging, there are also interpolation-free methods, which begin by sampling uniformly on a Cartesian, rather than polar grid. However, because fewer frequency samples are distributed along each direction in this case, it would not be an efficient use of the accelerated PO technique described in the previous chapter. Therefore, interpolation is used to translate to the Cartesian grid as shown in Figures 4.5.

Because of the band-limited nature of the frequency data, it is natural to use Fourier harmonics to interpolate along this dimension. Along each angular direction,

the radar cross section is interpolated by the Fourier series:

$$\sigma(k, \phi) = \sum_{m=0}^{M-1} c_m(\phi) e^{j2\pi m \tilde{k} \frac{M-1}{M}}, \quad (4.12)$$

where $\tilde{k} = (k - k_{min}) / (k_{max} - k_{min})$ is the scaled frequency. Note that the factor of $(M - 1)/M$ is needed, as otherwise $\exp(j2\pi m \cdot 1) \equiv 1$, which would in turn result in $\sigma(k_{max}, \phi) = \sigma(k_{min}, \phi)$. At the sampled angles, the coefficients c_m can easily be calculated by taking the Fourier transform of the equally-spaced frequency samples for that angle. To see this, note that in this case

$$\tilde{k}_m = \frac{m}{M-1}, \quad m = 0, 1, \dots, M-1, \quad (4.13)$$

so that (4.12) can be written as

$$\sigma(k_n, \phi) = \sum_{m=0}^{M-1} c_m(\phi) e^{j2\pi m n / M}. \quad (4.14)$$

This is a simple discrete Fourier transform, whose coefficients are given by

$$c_n(\phi) = \frac{1}{M} \sum_{m=0}^{M-1} \sigma(k_m, \phi) e^{-j2\pi m \tilde{k}_n \frac{M-1}{M}} \quad (4.15)$$

$$= \frac{1}{M} \sum_{m=0}^{M-1} \sigma(k_m, \phi) e^{-j2\pi m n / M}. \quad (4.16)$$

In the angular spectrum, where the Fourier harmonics are mostly applied to, the interpolated function is normally continuous, so that with a finite number of Fourier harmonics the interpolation can converge very well. The main complication here is that the scattered fields are unlikely to have the same value at the lowest and highest frequencies, leading to Gibb's phenomenon in the interpolation. When applying Fourier series to discontinuous functions, as in the case of the signal from

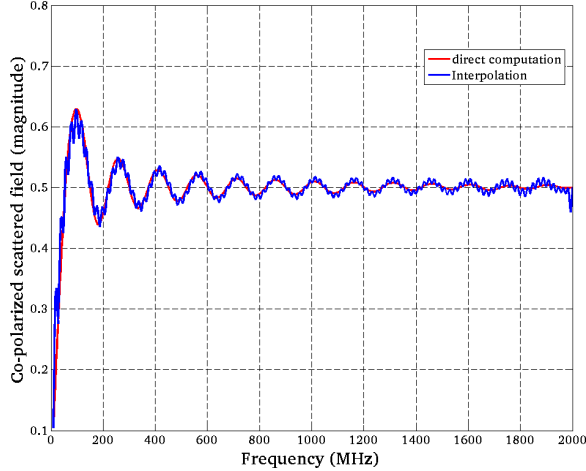


Figure 4.6: Interpolation with Fourier harmonics for sphere from 10 MHz to 1 GHz.

a frequency sweep, it is difficult to obtain a good approximation with a finite series of Fourier harmonics; if the number of terms is increased, the maximum overshoot moves closer to the discontinuity but is still present. To illustrate this issue, we simply simulate the co-polarized scattered field for a sphere with 1 meter radius from 12 MHz to 2 GHz with 30° elevation angle. Then we compare the direct PO solution with the interpolation using 115 harmonics, shown in Figures 4.6. The interpolation function, the blue line, is not smooth as the real scattered field, in red, due to the Gibbs's phenomenon.

To mitigate this effect, a few implementations can be done a top of the current interpolation, among which adding a windowing function and half range extension are most commonly used. Figures 4.7 shows the common even periodic extension for a discontinuous function $f(x)$. In this work we use even half range extension where the function f_1 is even and p -periodic. After the construction, the new function on the interval $0 < x < 2p$ is piecewise smooth and the coefficients can be found by

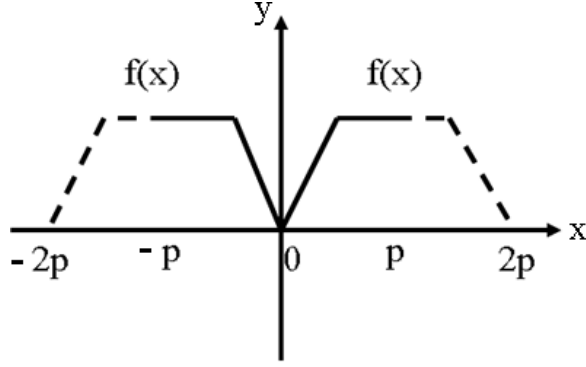


Figure 4.7: Even half-range periodic extension.

taking the DFT of the vector

$$[\sigma(k_0, \phi), \sigma(k_1, \phi), \dots, \sigma(k_{M-1}, \phi), \sigma(k_{M-2}, \phi), \dots, \sigma(k_1, \phi)]. \quad (4.17)$$

The interpolating function is then

$$\sigma(k, \phi) \approx \sum_{m=0}^{2M-3} c_m e^{j2\pi m \tilde{k}/2}. \quad (4.18)$$

Note that the factor of $(M - 1)/M$ is no longer needed, but it is necessary to divide \tilde{k} by 2, since we are only interested in the first half of the extension. Because of aliasing, it is also possible to generate different interpolating function. That is, instead of the frequencies running from 0 to $2M - 3$, they could go between $-M + 2$ to $M - 1$:

$$\begin{aligned} \sigma(k, \phi) \approx & \sum_{m=0}^{M-2} c_m e^{j2\pi m \tilde{k}/2} + \sum_{m=M}^{2M-3} c_m e^{j2\pi(m-2M+2)\tilde{k}/2} \\ & + c_{M-1} \cos [2\pi(M-1)\tilde{k}/2] \end{aligned} \quad (4.19)$$

Two points about (4.19) are that it will tend to be smoother than (4.18) due to the lack of higher frequency components. Also, the $(M - 1)$ -th harmonic has been replaced by a cosine, since the sine component is zero at the frequency sample

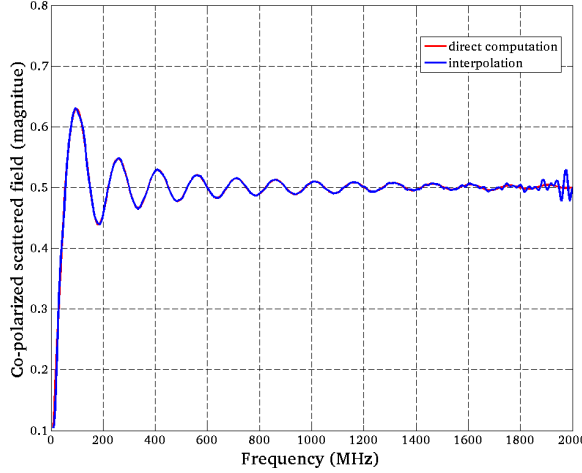


Figure 4.8: Interpolation with periodic extension for a sphere from 10 MHz to 1 GHz.

points. So, with the half range extension and series (4.19), the co-polarized field is interpolated again from 10 MHz to 2 GHz, as shown in Figures 4.8. The agreement is much better than the naive Fourier series except for the oscillation close to the maximum frequency, because the new constructed function is only C^0 continuous, i.e., the first derivative of the function is still discontinuous.

With all the interpolation done at each angle, the Fourier coefficients are pre-stored associate with angle. To evaluate at a given k, ϕ , we need to find two sample angles ϕ_1, ϕ_2 closest to ϕ and interpolate the mono-static field at ϕ angle:

$$\sigma(k, \phi) = \sum_{m=0}^M \left[c_m(\phi_1) + (c_m(\phi_2) - c_m(\phi_1)) \frac{\phi - \phi_1}{\phi_2 - \phi_1} \right] e^{j2\pi m \frac{k}{k_{max}} \frac{M-1}{M}}$$

Then with the interpolated Fourier coefficients, all the data point on the evenly-spaced Cartesian grid can be computed. Two different images shown in Figures 4.9

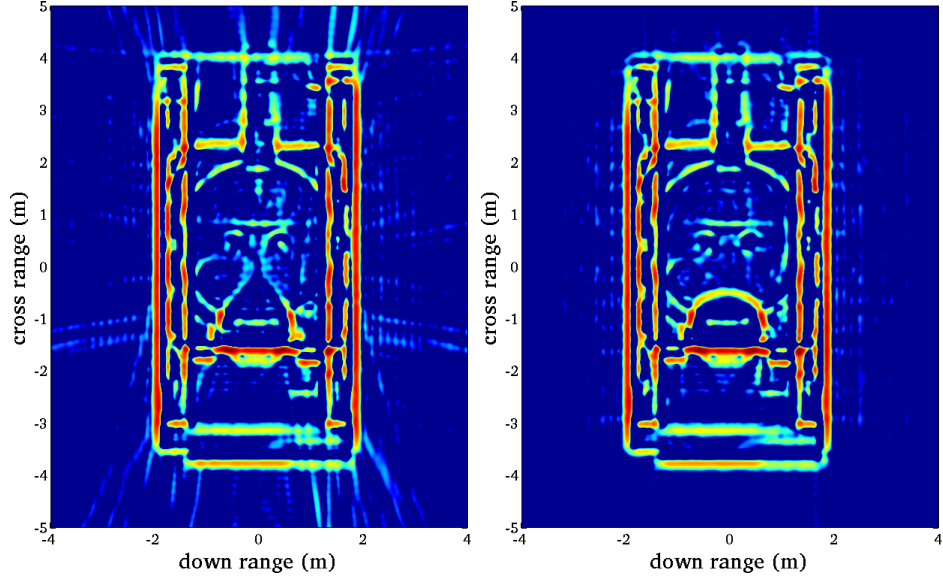


Figure 4.9: (a) Image generated without periodic extension for ZSU-23-4 with $f_{max} = 1 \text{ GHz}$. (b) Image generated with periodic extension for ZSU-23-4 with $f_{max} = 1 \text{ GHz}$

are generated for ZSU-23-4 from 12 MHz to 1 GHz with 0° elevation angle. First one is the image with fast PO solver and 2D acceleration sampling technique but the interpolation from polar to Cartesian grid is done without half range extension. More inaccurate features show up around and on the tank compared with the one generated based upon continuous periodic extension.

Chapter 5: Numerical Results

5.1 Image for simple object

In this section, we study two simple examples to verify the whole SAR imaging code used in this work. A sphere with 1 meter radius is first simulated from 10 MHz to 1 GHz with 0° elevation angle. With the 2D acceleration technique, the whole sphere is partitioned into 57 groups and within each group the number of sampling points are 12 in frequency domain and 38 in angular domain compared with 45*144 for the original problem. The computation for 2D spectrum and interpolation to Cartesian grid is done in 0.91s on an Intel E6750 duo core computer using OpenMP parallelization with 2 threads. The corresponding image is shown In Figures 5.1 and we can see the shape of sphere is perfectly reconstructed, but because of the limitation of resolution, the actual radius of sphere is around 1 meter with certain tolerance.

The second example is to construct a 1m*1m*1m cube from 10 MHz to 1 GHz with 0° elevation angle. The whole cube is partitioned into 70 groups, which require 14*46 sampling point for direct computation compared with 45*145 sampling points for the whole cube. Similarly to the sphere example, this is also done on the Intel E6759 duo core system with 2 threads, and total computation time is 0.39 s. The image generated from the interpolated spectrum is shown in Figures 5.2. We can see

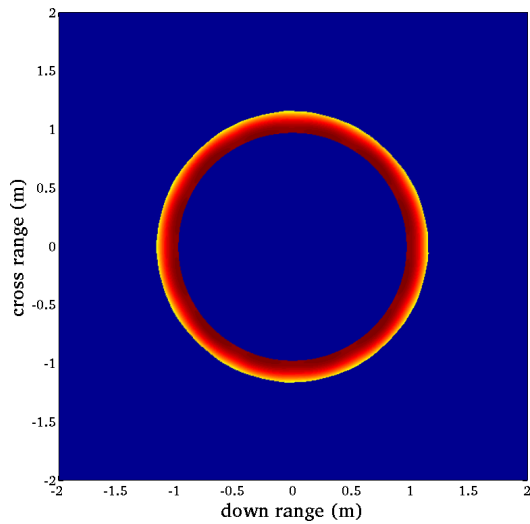


Figure 5.1: Image for a sphere with 1 meter radius.

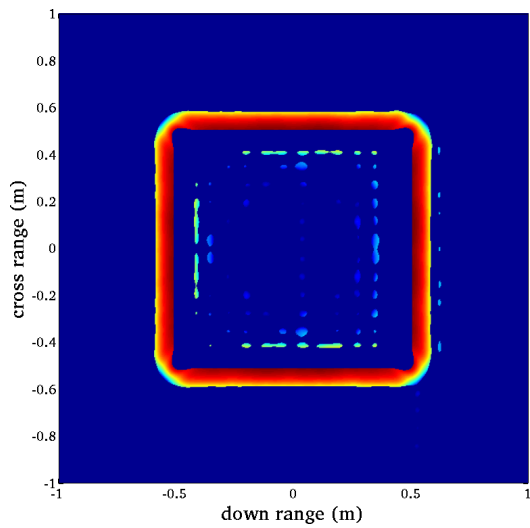


Figure 5.2: Image for a $1\text{m} \times 1\text{m} \times 1\text{m}$ cube.

the edges are constructed precisely but the four corners start to blur and intensity on the corner is much smaller than the edges. One possibility is the current solver only takes first order reflection into account, so the lack of diffraction mechanism causes the deficiency on the corner. Another issue in the current image for cube is the error inside the cube, which may due to the side lobes and the interpolation error.

5.2 SAR image for ZSU-23-4

With all the verification done in the previous section, SAR imaging for the complex object is considered here. The first example is to demonstrate the utility of the above methods is ZSU-23-4. The whole tank is adaptively meshed with 1,040,686 triangles. First of all, to validate the scattering pattern acceleration algorithm for complex object, the frequency range of interest is 12 MHz–1 GHz, and the angular sweep goes a full circle from 0° to 360° with 0° elevation angle. Given the Nyquist sampling rate 2, the number of samplings are 120 for frequency and 410 for aspect. If we use multi-frequency multi-angle acceleration algorithm, the whole object is divided into 430 groups to achieve the optimal complexity, and within each group the number of sampling points are reduced to $12*40$. And the total computation time is reduced from 5 h 35 m 49 s to 1m 4s using OpenMP parallelization with 8 threads.

Furthermore, the images are generated with the scattered field from direct computation and 2D interpolation. The difference between these two figures is barely noticeable as shown in Figures 5.3. After we show the validation of the current 2D acceleration algorithm for complex object, a more realistic situation is considered to generate the image for the tank. Since most of the SAR systems are working at

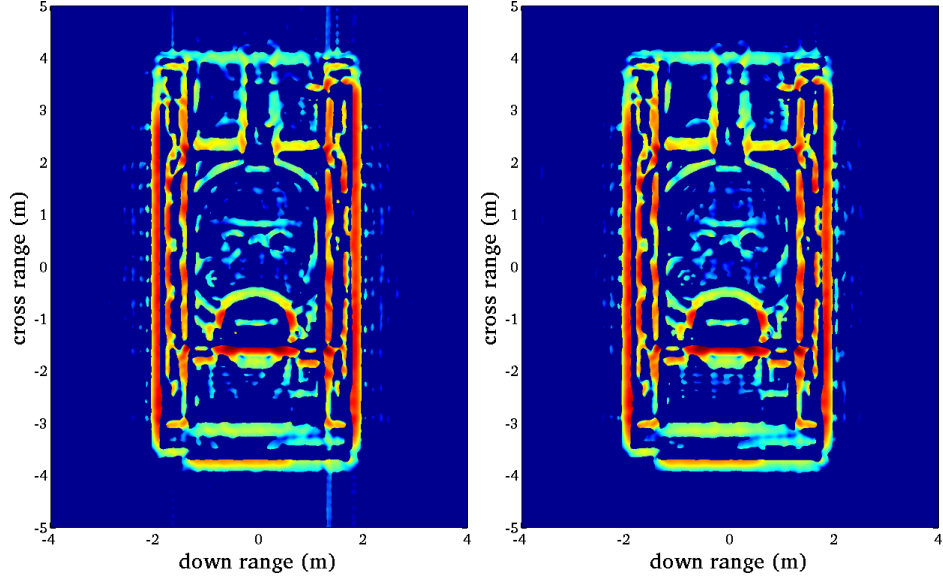


Figure 5.3: (a) Image generated from direct computation for ZSU-23-4 with $f_{max} = 1 \text{ GHz}$. (b)Image generated from 2D acceleration algorithm for ZSU-23-4 with $f_{max} = 1 \text{ GHz}$.

higher frequency at least X band for the better resolution of the target, the maximum frequency limit is increased from 1 GHz to 4 GHz then to 8 GHz. Figures 5.4 shows the image generated with 0° elevation angle with OpenMP parallelization on 8 threads. The total computation time is 33m 15 s with 430 partitioned groups, while the sampling number for each group is only $103*326$ compared with $1043*3283$ for the whole tank.

From the images at different frequencies, a better resolution can be observed and the small features start to show up at higher frequency for instance the details of tracks and wheels are visible in X-band image in Figures 5.4. Furthermore, a certain elevation angle is added on top of the image at X-band, since in the real life scenario the carrier of transmitter and receiver is not likely to rotate over target horizontally.

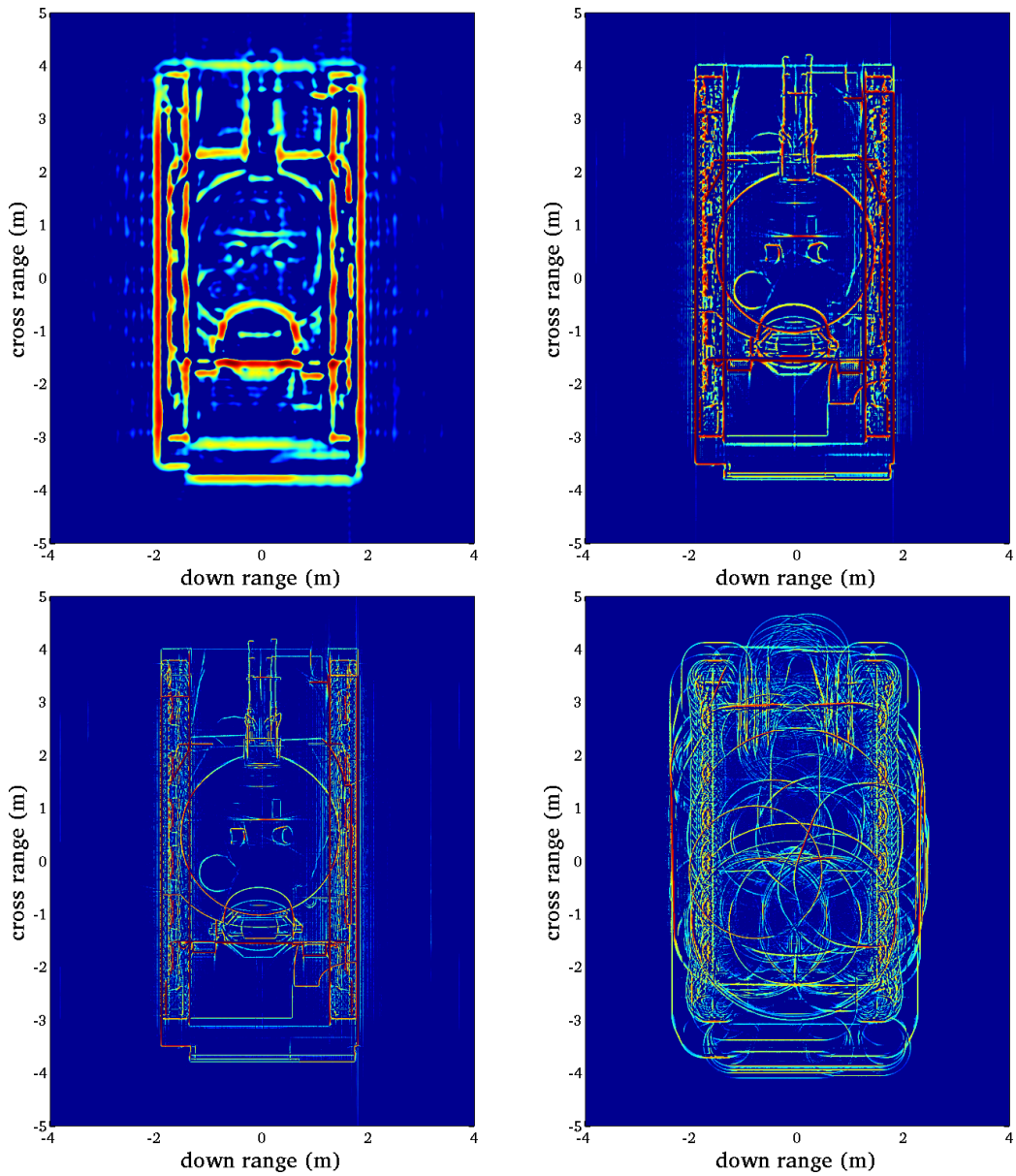


Figure 5.4: (a)Image for ZSU-23-4 with 0° elevation angle from 12 MHz to 1 GHz
(b)Image for ZSU-23-4 with 0° elevation angle from 12 MHz to 4 GHz (c)Image for ZSU-23-4 with 0° elevation angle from 12 MHz to 8 GHz (d)Image for ZSU-23-4 with 20° elevation angle from 12 MHz to 8 GHz

Table 5.1: Computation time on lit region identification with Z-buffer algorithm.

frequency range	12 MHz–1 GHz	12 MHz–4 GHz	12 MHz–8 GHz
angle sweep	0°–360°	0°–360°	0°–360°
elevation angle	0°	0°	0°
sampling points per group	12×40	51×163	103×326
# of groups	430	430	430
# of samplings for the entire tank	129×410	521×1641	1043×3283
computation time	1 m 4 s	9 m 33 s	33m 15 s
# of threads	8 (2 quad-core Intel E5520, 2.3 GHz)		

Hence, we study the tank image at 8 GHz with 20° elevation angle. Compared with the horizontal rotation image, the newly generated image shows more distortion on the edges and other features on top of the tank. All the computational statistics is listed in table on a 2 quad-core Intel E5520 workstation with OpenMP parallelization of 8 threads.

5.3 SAR image of f-16

Another interesting example that is shown here for SAR imaging is f-16 fight jet. Figures 5.5 (a) shows the real geometry we are using here, where the whole fight jet is considered as a pure PEC object. The object is meshed with 165,280 triangles and partitioned into 67 groups for the fast computation. In addition, the number of sampling points are reduced from 942*2971 to 31*100 for direct computation from 12 MHz to 1 GHz. The total computation time is 3m 22s and the corresponding image can be found in Figures 5.5.

From the current images generated at 0° elevation angle, the edges of the wings cannot be recognized clearly since the real structures in f-16 are close to thin plates.

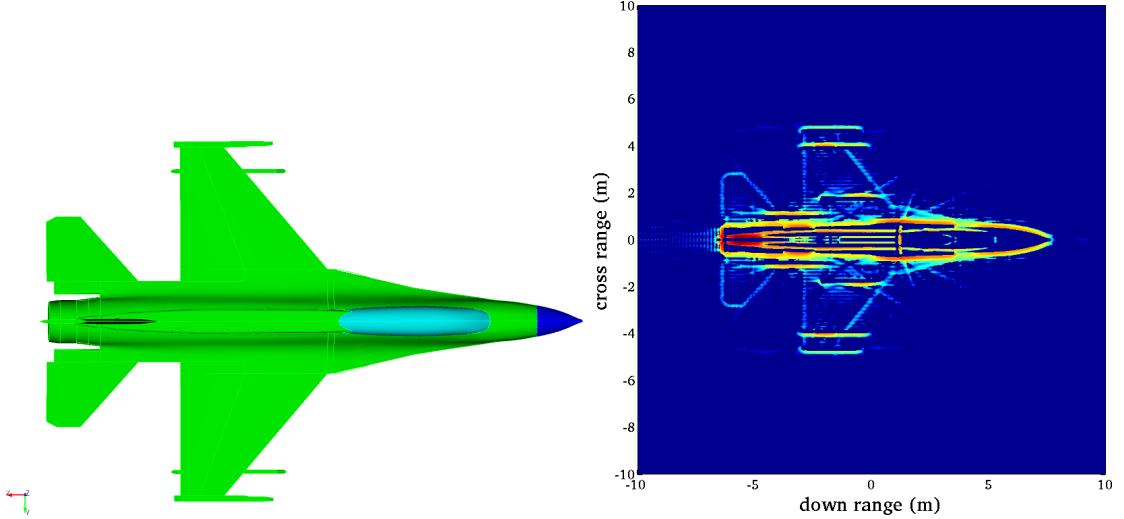


Figure 5.5: (a)f-16 geometry for SAR imaging. (b)Image for f-16 with 0° elevation angle from 12 MHz to 1 GHz.

If only first order PO solution is used for the scattered field without diffraction effects, those edges are really difficult to be detected from the horizontal rotation. As a comparison, the similar image is reconstructed from 12 MHz to 4 GHz with 20° elevation angle as shown in Figures 5.6. With a certain elevation angle, the horizontally thin structures like the wings become quite clear in the image. All the computational statistics for f-16 simulations on a 2 quad-core Intel E5520 workstation with OpenMP parallelization of 8 threads can be found in Table 5.2.

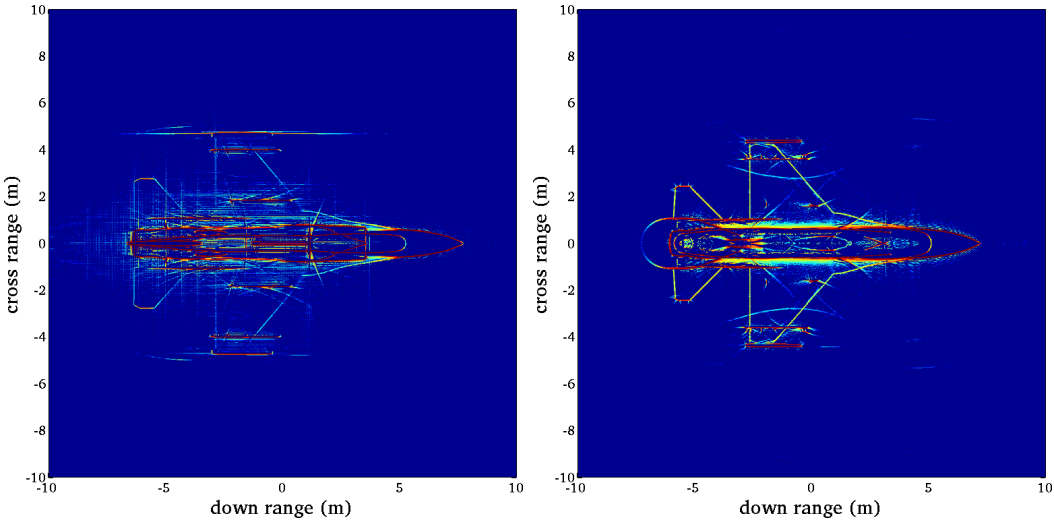


Figure 5.6: (a)Image for f-16 with 0° elevation angle from 12 MHz to 4 GHz. (b)Image for f-16 with 20° elevation angle from 12 MHz to 4 GHz.

Table 5.2: Computation time on SAR imaging for f-16.

frequency range	12 MHz–1 GHz	12 MHz–4 GHz
angle sweep	0° – 360°	0° – 360°
elevation angle	0°	0°
sampling points per group	31×100	127×401
# of groups	67	67
# of samplings for the entire f-16	233×742	942×2971
computation time	3 m 22 s	28 m 41 s
# of threads	8 (2 quad-core Intel E5520, 2.3 GHz)	

Chapter 6: Conclusions

In this thesis, the first order PO with self-shadowing technique has been introduced. Gordon's method together with acceleration schemes have been implemented to quickly compute the 2D frequency response of the target. Numerical results of complex objects such as ZSU-23-4 tank and F-16 fight jet were presented, which achieve good quality in SAR images and low computational costs.

For the further improvements, the effects of diffraction, multi-bounce and creeping waves need to be considered. And a more robust imaging model which can identify all of those scattering mechanism will be adopted. The effect of random lossy ground also needs to be taken into account in the future.

Appendix A: Proof for Gordon's method

Lemma: Let $\omega = [\omega_1, \omega_2]$ be a constant vector, Then

$$\iint_S e^{ik\omega \cdot x} dx_1 dx_2 = \frac{i}{k\omega^2} \int_{\partial S} e^{ik\omega \cdot x} (\omega_2 dx_1 - \omega_1 dx_2)$$

Proof: Apply Green's theorem (Stokes' theorem) to the right hand side

$$\begin{aligned} & \int_{\partial S} e^{ik\omega \cdot x} (\omega_2 dx_1 - \omega_1 dx_2) \\ &= \iint_S -\omega_1 \frac{\partial}{\partial x_1} (e^{ik\omega \cdot x}) - \omega_2 \frac{\partial}{\partial x_2} (e^{ik\omega \cdot x}) dx_1 dx_2 \\ &= -ik\omega^2 \iint_S e^{ik\omega \cdot x} dx_1 dx_2 \end{aligned}$$

Suppose now that S is an N -gon. Let $x(t) = (1-t)a_n + ta_{n+1}$ be the parametric representation of the n th side of S . The contribution of the n th side of S to the integral is :

$$\begin{aligned} & \int_0^1 (\omega^* \cdot \Delta a_n) \exp[ik\omega \cdot (1-t)a_n + ta_{n+1}] dt \\ &= (\omega^* \cdot \Delta a_n) e^{ik\omega \cdot a_n} \int_0^1 e^{ikt\omega \cdot \Delta a_n} dt \\ &= (\omega^* \cdot \Delta a_n) \frac{e^{ik\omega \cdot a_n}}{ik\omega \cdot \Delta a_n} (e^{ik\omega \cdot \Delta a_n} - 1) \\ &= (\omega^* \cdot \Delta a_n) \frac{e^{ik\omega \cdot a_n}}{ik\omega \cdot \Delta a_n} e^{ik\omega \cdot \Delta a_n/2} (2i) \sin\left[\frac{k}{2}\omega \cdot \Delta a_n\right] \\ &= (\omega^* \cdot \Delta a_n) \frac{\sin\left[\frac{k}{2}\omega \cdot \Delta a_n\right]}{\frac{k}{2}\omega \cdot \Delta a_n} \exp\left(\frac{ik}{2}\hat{\delta} \cdot (a_n + a_{n+1})\right) \\ &= T_n \end{aligned}$$

Bibliography

- [1] L. Lozano, M. Hernandez, C. Romera, I. Gonzalez, F. Saez de Adana, and M. Catedra, “Ray-tracing acceleration techniques to compute RCS of complex targets,” in *Antennas and Propagation Society International Symposium, 2004. IEEE*, vol. 4, June 2004, pp. 4495 – 4498 Vol.4.
- [2] C. Delgado, L. Lozano, O. Gutierrez, and M. Catedra, “Iterative PO method based on currents modes and angular Z-buffer technique,” in *Antennas and Propagation Society International Symposium 2006, IEEE*, July 2006, pp. 1853 –1856.
- [3] J. Kruger and R. Westermann, “Acceleration techniques for GPU-based volume rendering,” in *Visualization, 2003. VIS 2003. IEEE*, Oct. 2003, pp. 287 –292.
- [4] T. Balz and U. Stilla, “Hybrid GPU-based single- and double-bounce sar simulation,” *Geoscience and Remote Sensing, IEEE Transactions on*, vol. 47, no. 10, pp. 3519 –3529, Oct. 2009.
- [5] W. Gordon, “Far-field approximations to the kirchoff-helmholtz representations of scattered fields,” *Antennas and Propagation, IEEE Transactions on*, vol. 23, no. 4, pp. 590 – 592, Jul 1975.
- [6] P. Pouliquen and L. Desclos, “A physical optics approach to near field rcs computations,” *Ann. Telecomm.*, vol. 51, no. 5-6, pp. 219–226, 1996.
- [7] S. Legault, “Refining physical optics for near-field computations,” *Electronics Letters*, vol. 40, no. 1, pp. 71 – 72, Jan. 2004.
- [8] E. Papkeles, H. Anastassiou, and P. Frangos, “A time-efficient near-field scattering method applied to radio-coverage simulation in urban microcellular environments,” *Antennas and Propagation, IEEE Transactions on*, vol. 56, no. 10, pp. 3359 –3363, Oct. 2008.
- [9] S.-K. Jeng, “Near-field scattering by physical theory of diffraction and shooting and bouncing rays,” *Antennas and Propagation, IEEE Transactions on*, vol. 46, no. 4, pp. 551 –558, Apr 1998.

- [10] H. Ling, R.-C. Chou, and S.-W. Lee, “Shooting and bouncing rays: calculating the rcs of an arbitrarily shaped cavity,” *Antennas and Propagation, IEEE Transactions on*, vol. 37, no. 2, pp. 194 –205, Feb 1989.
- [11] R. Bhalla and H. Ling, “A fast algorithm for signature prediction and image formation using the shooting and bouncing ray technique,” in *Antennas and Propagation Society International Symposium, 1994. AP-S. Digest*, vol. 3, Jun 1994, pp. 1990 –1993 vol.3.
- [12] ——, “Three-dimensional scattering center extraction using the shooting and bouncing ray technique,” *Antennas and Propagation, IEEE Transactions on*, vol. 44, no. 11, pp. 1445 –1453, Nov 1996.
- [13] R. Bhalla, J. Moore, and H. Ling, “A global scattering center representation of complex targets using the shooting and bouncing ray technique,” *Antennas and Propagation, IEEE Transactions on*, vol. 45, no. 12, pp. 1850 –1856, dec 1997.
- [14] F. Obelleiro-Basteiro, J. Luis Rodriguez, and R. Burkholder, “An iterative physical optics approach for analyzing the electromagnetic scattering by large open-ended cavities,” *Antennas and Propagation, IEEE Transactions on*, vol. 43, no. 4, pp. 356 –361, apr 1995.
- [15] M. Sui and X. Xu, “A novel procedure for high resolution radar signature prediction of near field targets,” *Antennas and Propagation, IEEE Transactions on*, vol. 58, no. 9, pp. 2981 –2993, sept. 2010.
- [16] A. Boag and E. Michielssen, “A fast physical optics (FPO) algorithm for double-bounce scattering,” *Antennas and Propagation, IEEE Transactions on*, vol. 52, no. 1, pp. 205 – 212, jan. 2004.
- [17] S. Sefi, “Ray tracing tools for high frequency electromagnetics simulations,” Ph.D. dissertation, Royal Institute of Technology, Stockholm, Swedan, 2003.
- [18] P. Schniter, “Digital signal processing lecture notes: filters,” Ohio State University, 2011.
- [19] M. Hurst and R. Mittra, “Scattering center analysis via Prony’s method,” *Antennas and Propagation, IEEE Transactions on*, vol. 35, no. 8, pp. 986 – 988, Aug 1987.
- [20] A. Shaw and K. Naishadham, “ARMA-based time-signature estimator for analyzing resonant structures by the FDTD method,” *Antennas and Propagation, IEEE Transactions on*, vol. 49, no. 3, pp. 327 –339, Mar 2001.

- [21] A. Shaw, "Optimal identification of discrete-time systems from impulse response data," *Signal Processing, IEEE Transactions on*, vol. 42, no. 1, pp. 113 –120, Jan 1994.
- [22] J. Makhoul, "Linear prediction: A tutorial review," *Proceedings of the IEEE*, vol. 63, no. 4, pp. 561 – 580, april 1975.
- [23] K. Steiglitz, "On the simultaneous estimation of poles and zeros in speech analysis," *Acoustics, Speech and Signal Processing, IEEE Transactions on*, vol. 25, no. 3, pp. 229 – 234, Jun 1977.
- [24] V. Jain, T. Sarkar, and D. Weiner, "Rational modeling by pencil-of-functions method," *Acoustics, Speech and Signal Processing, IEEE Transactions on*, vol. 31, no. 3, pp. 564 – 573, Jun 1983.
- [25] A. Mackay and A. McCowen, "An improved pencil-of-functions method and comparisons with traditional methods of pole extraction," *Antennas and Propagation, IEEE Transactions on*, vol. 35, no. 4, pp. 435 – 441, Apr 1987.
- [26] Y. Hua, "On techniques for estimating parameters of exponentially damped/undamped sinusoids in noise," Ph.D. dissertation, Syracuse University, Syracuse, NY, August 1988.
- [27] T. Sarkar and O. Pereira, "Using the matrix pencil method to estimate the parameters of a sum of complex exponentials," *Antennas and Propagation Magazine, IEEE*, vol. 37, no. 1, pp. 48 –55, Feb 1995.
- [28] Y. Hua and T. Sarkar, "On SVD for estimating generalized eigenvalues of singular matrix pencil in noise," *Signal Processing, IEEE Transactions on*, vol. 39, no. 4, pp. 892 –900, Apr 1991.
- [29] F. Hu, T. Sarkar, and Y. Hua, "Utilization of bandpass filtering for the matrix pencil method," *Signal Processing, IEEE Transactions on*, vol. 41, no. 1, p. 442, jan 1993.
- [30] R. O. Schmidt, "A signal subspace approach to multile emitter location and spectral estimation," Ph.D. dissertation, Standford University, Standford,CA, 1981.
- [31] A. Barabell, "Improving the resolution performance of eigenstructure-based direction-finding algorithms," in *Acoustics, Speech, and Signal Processing, IEEE International Conference on ICASSP '83.*, vol. 8, apr 1983, pp. 336 – 339.

- [32] K. Wong and M. Zoltowski, “Root-MUSIC-based azimuth-elevation angle-of-arrival estimation with uniformly spaced but arbitrarily oriented velocity hydrophones,” *Signal Processing, IEEE Transactions on*, vol. 47, no. 12, pp. 3250 –3260, Dec 1999.
- [33] R. H. Roy, “ESPRIT-estimation of signal parameters via rotational invariance techniques,” Ph.D. dissertation, Standford University, Standford, CA, 1987.
- [34] R. Roy and T. Kailath, “ESPRIT-estimation of signal parameters via rotational invariance techniques,” *Acoustics, Speech and Signal Processing, IEEE Transactions on*, vol. 37, no. 7, pp. 984–995, Jul. 1989.
- [35] K. Naishadham and J. E. Piou, “A robust state space model for the characterization of extended returns in radar target signatures,” *IEEE Transactions on Antennas and Propagation*, vol. 56, no. 6, pp. 1742–1751, Jun. 2008.
- [36] S. Y. Kung, K. S. Arun and D. V. Bhaskar Rao, “State-space and singular-value decomposition-based approximation methods for the harmonic retrieval problem,” *Journal of the Optical Society of America*, vol. 73, pp. 1799–1811, 1983.
- [37] M. Fink and C. Prada, “Acoustic time-reversal mirrors,” *Inverse Problems*, vol. 17, pp. R1–R38, 2001.
- [38] C. T. L. Borcea, G. Papanicolaou and J. Berryman, “Imaging and time-reversal in random media,” *Inverse Problems*, vol. 18, pp. 1247–1279, 2002.
- [39] M. Yavuz and F. Teixeira, “Full time-domain DORT for ultrawideband electromagnetic fields in dispersive, random inhomogeneous media,” *Antennas and Propagation, IEEE Transactions on*, vol. 54, no. 8, pp. 2305 –2315, Aug. 2006.
- [40] D. S. C. Prada, S. Manneville and M. Fink, “Decomposition of the time reversal operator: Detection and selective focusing on two scatterers,” *J. Acoust. Soc. Am.*, vol. 99, no. 4, pp. 2067–2076, 1996.
- [41] H. Lev-Ari and A. Devancy, “The time-reversal technique re-interpreted: subspace-based signal processing for multi-static target location,” in *Sensor Array and Multichannel Signal Processing Workshop. 2000. Proceedings of the 2000 IEEE*, 2000, pp. 509 –513.
- [42] E. Marengo, F. Gruber, and F. Simonetti, “Time-reversal MUSIC imaging of extended targets,” *Image Processing, IEEE Transactions on*, vol. 16, no. 8, pp. 1967 –1984, Aug. 2007.

- [43] M. Yavuz and F. Teixeira, “Space-frequency ultrawideband time-reversal imaging,” *Geoscience and Remote Sensing, IEEE Transactions on*, vol. 46, no. 4, pp. 1115 –1124, April 2008.
- [44] C. A. Balanis, *Advanced Engineering Electromagnetics*. John Wiley & Sons, Inc, 1989.
- [45] F. Vico-Bondia, M. Ferrando-Bataller, and A. Valero-Nogueira, “A new fast physical optics for smooth surfaces by means of a numerical theory of diffraction,” *Antennas and Propagation, IEEE Transactions on*, vol. 58, no. 3, pp. 773 –789, march 2010.
- [46] O. Conde, J. Perez, and M. Catedra, “Stationary phase method application for the analysis of radiation of complex 3-D conducting structures,” *Antennas and Propagation, IEEE Transactions on*, vol. 49, no. 5, pp. 724 –731, May 2001.
- [47] A. Boag, “A fast physical optics (FPO) algorithm for high frequency scattering,” *Antennas and Propagation, IEEE Transactions on*, vol. 52, no. 1, pp. 197 – 204, Jan. 2004.
- [48] M. Soumekh, *Synthetic Aperture Radar Signal Processing with MATLAB Algorithms*. John Wiley & Sons, Inc, 1999.
- [49] H. Stark, J. W. Woods, I. Paul, and R. Hingorani, “An investigation of computerized tomography by direct fourier inversion and optimum interpolation,” *Biomedical Engineering, IEEE Transactions on*, vol. BME-28, no. 7, pp. 496 –505, july 1981.
- [50] J. D. O’Sullivan, “A fast sinc function gridding algorithm for fourier inversion in computer tomography,” *Medical Imaging, IEEE Transactions on*, vol. 4, no. 4, pp. 200 –207, dec. 1985.